Deep ultraviolet-excited fluorescence histology with fibre optic illumination for tissue microtopography and quantitative mapping

Alexander Si Kai Yong*, Ko Hui Tan*, Chiyo Wan Xuan Tan*, Joel Lang Yi Ang, Jessica Sze Jia Kng, Cyrus Jia Jun Tan, Rachael Hui Kie Soh, Rachel Yixuan Tan, Kaicheng Liang

Dec 2022

1 Abstract

Rapidly resolving microstructure and function from thick biological samples is a critical requirement from basic research to clinical diagnosis. The need for physical sectioning leads to limitations in the speed, cost, or ease of sample preparation and imaging. We introduce a fluorescence microscope with deep ultraviolet illumination via omnidirectional fibre optics, based on the concept of microscopy with ultraviolet surface excitation (MUSE). We further exploited precise control of directional illumination to produce 3D reconstructions of surface microtopography from 2D images. Our technology is applicable to diverse sample types, ranging from single cells and 3D cultures to large tissue samples while utilising conventional, widely available objective lenses in a compact and portable implementation (30 cm by 30 cm). We demonstrated the use of our microscope with important fluorescent assays through quantitative viability studies in single cells to whole organs, organ-level studies comparable to standard H&E histology, and multiplexed immunohistochemistry staining. We also explored the potential for microtopography to provide additional insight into vascular and tissue texture and heterogeneity studies. This technology fills long-standing technological gaps in both the laboratory and clinic for a general-purpose microscope that is simple, portable, and cheap that can provide near real-time biological insights.

2 Introduction

Fluorescence imaging of large unsectioned biological samples is a key enabler in protein expression studies [1] as well as emerging efforts in spatial transcriptomics at the organ level [2]. Confocal microscopy, and more recently light-sheet microscopy with tissue clearing, are the conventional techniques used today. However, these techniques are highly time-consuming or laborious, particularly if comprehensive spatial insights at the 'mesoscopic' centimetre scale are of interest. These technical demands are beginning to mirror the needs of surgery or clinical procedures in which tissue is excised for microscopic evaluation, and where intraoperative real-time feedback promises actionable insights for clinicians - an oft-cited scenario that has been vigorously tackled by biophotonics engineers [3]. The requirements of rapid optically-sectioned imaging of thick bulk samples at high resolution on a compact and economical platform are also welcomed in the context of the life sciences which have even more stringent requirements on quantitative imaging, molecular specificity, and compatibility with available laboratory assays [4].

While microscopy of extremely thin (a few microns thick) samples using brightfield illumination is an age-old technique, more sophisticated optical methods for imaging thick unsectioned tissue have been pursued in earnest in recent decades. There exist limitations for microscopic analysis of tissue histology by conventional hematoxylin and eosin (H&E) staining, with significant drawbacks in its time-consuming multi-step protocol as well the need for continuous sectioning for thick samples [5, 6]. Label-free microscopy of microstructures based on optical coherence tomography [7, 8] or quantitative phase imaging [9] is attractive for their simplicity in sample preparation and non-destructive nature, but the lack of molecular multi-colour contrast hampers image interpretation and multiplexed readouts. Fluorescence imaging leverages molecular contrast (either intrinsic or exogenous) and potentially generates a closer analogue to conventional histopathological assays. Additionally,

optical sectioning techniques facilitate fluorescence microscopy of thick samples. Confocal microscopy [10] and multi-photon microscopy [11] are capable of high axial resolution in tissue and have been proposed as potential intraoperative systems. However, the requirement of physical scanning limits the speed, and the high cost, sheer size, and complexity of such laser scanning microscopes limit their use to privileged scientific or clinical communities. Structured (including HiLo) illumination for the rejection of out-of-focus light has also been successful on thick biomedical samples [12, 13].

The use of deep ultraviolet (DUV) light at 200-300 nm (also known as UV-C) for fluorescence excitation is a recent promising approach for tissue microscopy and has several advantages including the use of light-emitting diodes (LEDs) instead of lasers for the excitation of multiple fluorophores at once, and superficial penetration in tissue providing intrinsic depth confinement for optical sectioning [14, 15]. Also known as microscopy with ultraviolet surface excitation (MUSE), this technique's simplicity has been previously highlighted for its potential in intraoperative imaging [16, 17], although demonstrations in the life sciences have been fewer [18, 19]. However, the requirement for DUV excitation at an angle oblique to the optical detection path (due to poor transmission of DUV through standard glass) and direct illumination by LEDs has demanded the use of infinity-corrected long working distance objective lenses, which are remarkably costly and large, and further warranting using a tube lens. This esoteric requirement also greatly hinders the use of switchable objective magnifications–a mainstay of most microscopes and critical for both biological microscopy and histopathology assessment.

We have developed a compact and portable microscope based on MUSE that aims to solve a broad swathe of rapid and high-throughput imaging needs of tissue at the organ scale, featuring applications in the life sciences and potentially translatable to surgical point-of-care. The 30 x 30 cm^2 platform utilized multiple optical fibres on a custom 3D printed optomechanical mount for omnidirectional DUV illumination, which not only solved the problem of oblique light delivery via a short working distance but also provided a unique capability to obtain micro-scale 3D topographic mapping using the classic photometric stereo algorithm [20]. We used stepper motors with micrometre stages to produce large stitched (mosaiced) images of samples up to 1.5 cm^2 in size. Our technology has been demonstrated with 2-colour tissue staining as an analogue to clinical H&E staining, and with immunohistochemical fluorescence with multiplexing of 2 colours. As a further proof-of-concept as a powerful tool for tissue biology, we performed a quantitative study of the effects of antibiotic drug insult on kidney organ viability.

3 Results

3.1 Fibre optic illumination

The microscope sample was illuminated by 4 multi-mode fibres coupled to DUV LEDs (Fig. 1a, Supp. Fig. S1), a distinctly different approach over previous MUSE designs that had LEDs pointing directly at the sample (either with or without lensing or with rigid light guides) via a large space clearance afforded by long working distance objectives [21]. Fibre optic illumination enabled the use of low-cost OEM microscope objectives (Edmund Optics) originally intended for generic inspection applications with working distances as short as ~ 1 mm at 10X magnification (Fig. 1b). These objectives were finite conjugate and Deutsche Industrie Norm (DIN) standard, requiring a simple optical path comprising a light-tight tube between the objective and camera, with no tube lens necessary. This illumination design also allowed the LEDs to be mounted on the base at a distance from the sample, providing better heat management and space maximization. The optical fibres were held by a custom-designed 3D-printed optomechanical mount that had up to 4 degrees of adjustment freedom to optimize the illumination direction for each fibre. Each mount could be optimised for an objective of a particular magnification and working distance, and be easily hot-swapped. We implemented both the commonly used MUSE magnification of 10X as well as a 4X option for faster imaging over large fields.

3.2 Biomedical applications from cells to tissue

While the capability of MUSE (Fig. 1c) to image unsectioned tissue and its potential in clinical applications is well documented, less has been explored in the life sciences such as the myriad of microscopy demands in cell and molecular biology. We found DUV excitation well-suited for visualising a wide range of fluorescent-stained biological sample assays. The few notable exceptions that did not appear to adequately fluoresce under DUV are calcein AM (live cell stain), certain Alexa Fluors, and certain fluorescent proteins. Among countless

possibilities, we chose to demonstrate several applications of one of the most important assays used in biology - the investigation and quantification of cell and tissue viability [22, 23]. As an alternative to the popular calcein AM and ethidium homodimer assay [24], we used SYTO 9 and propidium iodide for live and dead cell staining respectively. While this combination is marketed by Invitrogen primarily as an assay for bacteria, these dyes are also well-documented to work effectively on eukaryotic cells [25].

Conventional viability measurements use fluorescent plate readers, which give fluorescence intensity readouts summed over entire samples but have no spatial information or cell-level statistics. To demonstrate a fast image-based viability assay, 70% ethanol was added to attached MCF-7 cells stained with SYTO 9 and propidium iodide and images at multiple time point up to an hour were captured (Fig. 1d). Image analysis yielded a quantitative viability assessment based on cell segmentation and counting, which was likely more representative than summed intensity readouts. The same viability assay was also applied successfully to 3D culture and fresh tissue and yielded sharp cellular images from the surface (Fig. 1e-f). DUV excited fluorescence is a faster and more accessible alternative to confocal microscopy for obtaining a readout at cellular resolution and delivering higher quality results than conventional widefield imaging with visible light excitation.

The microscope is particularly well suited to large millimetre-scale samples such as studies of tissue and organs (Fig. 1i-l). In protocols designed to accommodate rugged clinical scenarios such as biopsy sampling or surgical resection, tissue were manually cut with a sharp blade into small pieces (a few mm up to $\sim 1cm$ in width), then stained for under a minute with fluorescent labels and mounted in a modified tissue cassette with a quartz glass viewing window. Fluorescent colours may be remapped to a clinically relevant stain appearance such as H&E [26, 27] (Fig. 1i). For benchtop biological investigations, tissue were either manually cut or sectioned with a vibrating microtome into thick $\sim 700\ \mu m$ slices (Supp. Fig. S2). We demonstrated the capability of studying protein expression by labelling extracellular matrix proteins in the mouse uterus using immunohistochemistry (Fig. 1j).

3.3 Histological studies at organ level

Prior MUSE work had shown close correspondence between DUV-excited fluorescence imaging of tissue samples and histology [15]. For validation of our microscope design against the state of the art of image quality, we selected three organ systems for study - the female reproductive tract, renal and digestive systems (Fig. 2-3). We focused on fresh samples, which have strong relevance to both clinical applications and biological viability studies. We also systematically collected image examples at both 10X (standard MUSE magnification preferred for clinical histology by prior studies) and 4X, the latter also showing excellent nuclear visualization but at larger fields. Microscopic quantification such as the measurement of vascular structures, staging of follicles, and functional features of the uterus could be performed. As an aside, we note that fixed samples had clearer preservation of cellular details and closer correspondence to histology, but were incompatible with fresh preparations.

The rat cervix is a large structure with complex organization showing folds, mucosal layering, vasculature and ductal entrances (Fig. 2a-b). The quasi-3D effect of oblique illumination provided a useful perspective of the organ such as the inner surface of the endometrium. The layer of simple columnar epithelial cells lining the endometrium corresponded well to histology. Large field of view coverage at microscopic resolution enabled quantitative measurements at the organ scale that could correlate with physiology or phenotype, such as the size of a follicle indicating maturation (Fig. 2c-e), and endometrial thickness as a marker of estrus cycle staging (Fig. 2f-k).

We present detailed kidney histology as well as viability studies discussed later. Renal corpuscles including the Bowman's capsule and glomerular vasculature were well visualized, and vascular parameters such as calibre and wall thickness/friability could be assessed (Fig. 3a-e). Blood vessels were particularly compelling for the microtopographical study. The stomach was also particularly interesting because it had both mucosal and muscular histology (Fig. 3f-n), and had relevant pathology for both inner and outer surfaces. Although MUSE is primarily a surface imaging modality, cross-sectional layer architectures such as the gastric mucosa could be studied with a 'Swiss roll' preparation of tissue rolled up and mounted on its side (Fig. 3f-h). High-quality *en face* views of gastric pit openings or outer muscle were simple to obtain (Fig. 3l-n).

3.4 Fluorescence microtopography

Previous MUSE reports had observed that the images, while 2-dimensional, had a quasi-3D effect due to the unsectioned tissue having surface structure and the oblique illumination producing shadows and some perception of depth [15]. We further exploited this effect to generate a complete 3D reconstruction of the sample surface topography at microscopic resolution, using the photometric stereo algorithm (Fig. 1g-h, Fig. 4a-b). This classic computational technique enabled depth reconstruction from a single fixed field of view using fluorescence images excited from multiple different fibre optics directions about the optical axis (Fig. 4e-f). Additionally, our fibre optic illumination strategy uniquely enabled different angles and directions of illumination to be achieved. The highly oblique illumination angles provided strong shading that prominently highlighted both large microstructural features such as tubules/ducts and more minute textural differences that could be associated with cellular heterogeneity. The illumination from each optical fibre was used to generate surface topographical information (Fig. 4g-j), which would otherwise be unobtainable from thin-sectioned tissue or brightfield microscopy, and could be rapidly obtained without the need for more complex 3D optical techniques.

We validated the imaging of a simple cell spheroid against confocal microscopy, an established 3D imaging technique (Fig. 4c-d). Corresponding features between the obtained 3D depth map and confocal image were qualitatively matched, highlighting the accuracy of MUSE microtopography by photometric stereo. Quantitative depth measurements and exact surface normal vectors can be obtained (Fig. 4g-h), in principle, if given the exact illumination angles. However, in practice, LED (and fibre optic) illumination has a large divergence angle, so it may be more feasible to calibrate depth against a standard 3D technique. Additionally, the illumination intensity may differ between fibre optics, due to variations in the DUV LED intensity and fibre optic coupling efficiencies limiting the micro topography render to a highly accurate but imperfect model. While histogram matching can force a more uniform lighting intensity among images, possible differences between samples due to slight variations in the fluorescence staining conditions further limit the ability of the microscope to attain true depth values between samples.

MUSE microtopography was able to recapitulate the surface contour and finer micro-surface features. As a proof of concept, we imaged fixed liver samples, where we reconstructed the 3D structure of blood vessels and surface irregularities from the liver sinusoidal organisation (Fig. 4a, i). Features such as the inner wall of blood vessels and the uneven hepatic surface of the liver sinusoids could be observed. The ability to resolve differences in micro-surface topography provided additional information which would be otherwise unobtainable from standard tissue histopathology.

3.5 Investigating antibiotic insult to kidney viability

Our platform is able to support highly efficient imaging for a wide array of biological studies. We investigated organ-level physiology, specifically the assessment of antibiotic insult to kidney tissue viability. The kidney functions as a major excretory organ for the concentration and elimination of metabolic waste from the body. Most drugs and their metabolites are also eliminated by the kidneys through renal excretion. Kidneys are thus an easy target of drug toxicity effects [28–30]. The use of vancomycin remains as a standard for treatment of methicillin-resistant Staphylococcus aureus (MRSA) [31] despite being linked to nephrotoxicity and acute kidney injury (AKI) for decades [32–34]. Previous studies had investigated the effects of vancomycin on kidney structure and function, *invitro* cell-level changes in viability, as well as mechanistic studies [22, 35–38], but there has yet to be a visual representation of kidney tissue viability, apart from area-specific images from Crawford *et al.* [35]. We demonstrate a simple method for large kidney tissue viability imaging, with exposure to vancomycin as an insult.

Kidneys were harvested from sacrificed mice and longitudinally sectioned into 700 μm slices, before exposure to vancomycin (5 mg/mL and 10 mg/mL). A total of 18 mid-kidney slices were obtained from 6 harvested kidneys. The lower dose of vancomycin corresponds to the dosage used for vancomycin treatment in humans as well as *invivo* and *invitro* studies of vancomycin effects [30, 38–41]. Kidney slices were subjected to vancomycin insult for an hour with PBS as the control. The slices were then washed, stained and mounted on our custom cassette fitted with a quartz cover slip before being imaged on our microscope at 4X magnification (Fig. 5a, d, h). The whole tissue, renal corpuscle, and proximal convoluted tubule viabilities were then quantified (Fig. 5i). The methodology of the viability experiment is summarised in Fig. 5g. The viability generally decreased with an increased dose of vancomycin. Across all groups, we found that the viabilities of proximal convoluted tubules

were higher than that of the renal corpuscles. The increased vancomycin exposure decreased the viability of the tissue, displaying similar trends shown in [22, 36, 37, 42]. An advantage of whole-tissue viability imaging is the ability to compare intra-tissue and inter-tissue variance in regions of interest. We hypothesise that the increased vancomycin dosage is related to the number of discernible corpuscles. This could be due to the alterations in the tissue structure caused by the insult [43]. In addition, it was observed that there exists intra-tissue variation in viability, with additional inter-tissue variance between samples in the treatment groups. Figure 5k compares the variance of viability in all renal corpuscles in the 6 control kidney slices.

Our microscope presents a unique capability for large tissue imaging of stained samples. Viability can be assessed with stained samples and quantification can be performed on images obtained. The synergy of tissue cell-level viability observation and corresponding fluorescence quantification would not be possible using a microplate reader. Our microscope has all-rounded capabilities in *ex vivo* tissue imaging requirements.

4 Discussion

MUSE has been rightly celebrated for its simplicity in concept - the combination of oblique DUV illumination and widefield detection. However, prior published illustrations of real-world implementations [17, 18, 21, 44] showed inevitably large and complex setups, with the notable exception of Pocket MUSE albeit its incompatibility with large surgical or mesoscale samples [19]. Our concept of fibre optic-delivered DUV illumination was not only space-conserving but also enabled a number of technical innovations that significantly expand the capabilities of MUSE. Light delivery via a set of small diameter and easily micro-positioned fibre tips greatly relax requirements for long working distance objective lenses, and the resultant simplification of the optical path led to an extremely compact space footprint. Multiple sets of optical fibres could be configured for the switching of objectives at different magnifications, allowing us to show results not only at the standard 10X magnification but also fast and high-quality large-field mosaics at 4X. We anticipate these concepts to broaden options for cost-effective MUSE design and implementation across both clinical and biomedical scenarios.

Researchers have appreciated the phenomenon of meaningful shadowing that was produced by oblique DUV illumination, which generated a pseudo-3D effect from coarsely-cut samples and organ surfaces [15]. While the omnidirectional illumination enabled by our fibre optic approach would at least improve uniformity, we further exploit directional illumination control to produce full 3-dimensional surface reconstruction using the well-known photometric stereo algorithm [20]. Fluorescence is typically assumed to be Lambertian (isotropic) [45] and has been previously studied as a feasible modality for photometric stereo reconstruction [46]. The ability of MUSE to exclude illumination via imaging optics further protects images from non-Lambertian reflectance artefacts. Our study is likely the first to demonstrate photometric stereo reconstruction of fluorescence at a microscopic level. This could have applications in rapidly evaluating the 3D morphology of organoids and 3D culture as they gradually form microstructures of interest, as well as assessing texture and roughness of organ surfaces or tumours, which has been reported in other imaging modalities to be a metric of cellular heterogeneity and could have future relevance as a malignancy marker in histopathological evaluation [47, 48]. The ability to distinguish variations in the surface features at the micro-scale could be of value for research and clinical use cases.

While we emphasize the ability to infer histological and biological insights in a large region of interest without the need for sectioning, being constrained to surface-level information can be restricting for 3D biological samples; 3D information beyond surface texture is largely unobtainable. We were also only able to image excised samples, limiting our study to only *ex vivo* imaging. Additionally, imaging at higher levels of magnification ($\sim$40x) with our specific range of objectives involves even shorter working distances and likely requires more sophisticated illumination strategies if not intrinsically limited by the DUV penetration depth. Finally, more exploration into quantitative measurements can be done, from the prevalence of immunohistochemically stained protein expressions to exact depth measurements from microtopography measurements.

Although multiple studies have already shown MUSE to generate exquisite images from unsectioned fresh or fixed tissue, our study also featured a number of examples. This is partly to demonstrate our unique optical design with no-brand lensing to be competitive with the state of the art, and also to present a few new perspectives - namely, the thorough histological study of specific organ systems, and quantitative studies of fluorescence images, both of which are particularly crucial for applications in translational biology. While we acknowledge that fixation is ideal for the visualization of tissue structures and is also compatible with DUV excitation, our focus is to feature fresh (relatively live) biological preparations which are necessary for important viability quantifications, and also help to define an important translational step towards the envisioned use of DUV

excitation on live samples and *in vivo* models. MUSE is conceivable as a potential non-destructive modality with applications in both biology and medicine. Even as the toxic/mutagenic effects of DUV light are well documented, the very brief sub-second exposures needed for high-quality imaging may be tolerable by living systems and certainly justify future dosing studies. Given concurrent advances in DUV light sources, fibre optics and microscopy, the potential of minimally invasive ultraviolet endoscopy [49] for real-time cellular interrogation of living organs is due for a revisit.

5 Methods

5.1 Microscope design and components

The DUV fibre optic fluorescence microscope platform was based on epi-illumination inverted microscopy. The microscope sat on a 30 x 30 cm optical breadboard (Edmund Optics) and comprised the illumination, optical, sample holder, and mechanical and electrical components.

Illumination components DUV illumination at a peak wavelength of 277 nm was produced by DUV LEDs powered by a constant 700 mA current supply (RECOM) and heatsinked (Intelligent LED Solutions) to prevent overheating. Magnetic butt-coupling of multimode optical fibres (Edmund Optics) to the LEDs directly was achieved with a custom 3D-printed magnetic fibre coupler (Supp. Fig. S1). The magnetic coupler allowed hot swapping of the illumination source and the optical fibres. The magnetically butt-coupled optical fibres had a measured output power of around 0.04 mW and a coupling efficiency of roughly 5% of the measured LED output power. Up to 2 fibre optics were coupled to a single LED, although the combined coupling efficiency remained at roughly 5%. The power output was corroborated by 2 power meter measurements (Thorlabs, Hamamatsu). The opposing DUV-emitting end of the fibre optic was controlled via a 3D printed custom optomechanical fibre holder jig which provided 4 degrees of freedom, allowing fine control and angle adjustments of the fibre to be made for uniform sample illumination.

Optical components Digital images were taken using a colour camera (Teledyne FLIR) magnified by either 10X or 4X finite conjugate DIN objectives (Edmund Optics). The numerical aperture and working distances for the 10X and 4X objectives were 0.25, 1.5 mm and 0.10, 15.25 mm respectively. A custom 3D-printed objective holder was non-mechanically coupled to a shortened focal tube (Edmund Optics), enabling hot swapping between the 10X and 4X objective setups. The objective holder included a filter slot which enabled the suppression of specific wavelengths which could minimise unwanted signals like autofluorescence from samples. The focal tube connected the objective holder with the colour camera and provided an optically isolated path for the emitted signal of the sample to be detected by the colour camera which functioned as the imaging system sensor. The effective resolution was measured to have a 13.6% contrast level at Group 9 Element 1, corresponding to a resolution of 0.977 μm (10X), and 12.0% contrast level at Group 7 Element 4, corresponding to a resolution of 2.76 μm (4X) by imaging a USAF 1951 resolution target. The clear resolution target was imaged by placing a piece of plain white paper behind the resolution target. The autofluorescence of the plain paper, in the presence of the DUV excitation, provided the backlight illumination of the resolution target. The effective field of view was determined to be 0.748 by 0.561 mm (10X) and 1.85 by 1.39 mm (4X) by imaging a checkerboard calibration target.

Sample holder components Histology cassettes and 6-well plates, both modified to include a 250 μm thick UV-transmissible quartz window, were used to contain tissue and cell samples respectively. A custom-machined steel sample holder supported by 4 optical posts was used to mount the histology cassettes and 6-well plates. The standard histology cassettes were modified by cutting a hole approximately 11 mm by 20 mm before applying liquid epoxy to adhere a quartz coverslip (JGS2, Latech) to the outer surface covering the hole. The quartz coverslips acted as a flat and UV-transmissible surface for samples to be placed on for imaging. The 6-well plates (3516, Corning) were similarly modified by drilling a 7 mm hole through the bottom of each well and having the quartz coverslip cover the hole using liquid epoxy. This created a surface for cell samples to be seeded, incubated, and imaged on, without the need for disruptive detachment by trypsinisation for imaging on a separate holder.

Mechanical and Electrical Components X-axis and Y-axis movement at submicrometer precision of the sample relative to the camera was enabled by mounting the sample holder on a stack of 2 manual linear translation stages. Z-axis movement was enabled by attaching the optical components to a manual vertical

translation stage. 2 3D printed stepper motor holders and stepper motor couplers were designed to co-axially couple the stepper motors with the micrometre knob of the stage. A microcontroller controlled the motor by either parsing a set of sequential instructions for automated stage movement or inputs from an analogue stick for manual stage movement.

5.2 Biological applications

Biological sample preparation Human breast adenocarcinoma epithelial MCF-7 cell line was purchased from the American Type Culture Collection (ATCC). Cells were cultured in RPMI Medium 1640 (22400089, Gibco) supplemented with 10% fetal bovine serum (FBS-HI-12A, Capricorn Scientific), 100 U/mL penicillin and 100 $\mu g/mL$ streptomycin (15140-122, Gibco) in 5% CO2 at $37°C$. Formation of spheroids was induced by seeding MCF-7 cells at 2 x 10^4 cells/well, in 24-well F-bottomed ultra-low attachment plates (174929, Life Technologies) with shaking for 2-3 days. For tissue samples, female NCr nude mice were euthanized and dissected. Organs were harvested and washed in 1X Phosphate Buffered Saline (PBS) (BUF-2040-10X4L, 1st BASE), and sliced either using a vibratome (VF500-0Z, Precisionary Instruments) or manually using a scalpel depending on the use case. For vibratome slicing, the organ was embedded in 2% Type I-B agarose (Sigma Aldrich). In brief, the sample was glued onto the plunger of the specimen tube, liquid agarose was pipetted in excess to cover the tissue before the agarose was solidified using a chilling block. The specimen tube containing the sample was loaded onto the vibratome and sliced into 700 μm to 1 mm-thick slices at various oscillation and sectioning speeds depending on the organ type. Surrounding agarose was delicately removed using forceps before staining, with Hoechst and Rhodamine B for histological studies or SYTO 9 and propidium iodide for viability studies (Figure 7).

Histological studies Hoechst 33342 (62249, Thermofisher Scientific) and Rhodamine B (A5102, TCI) histology-like fluorescence stains were prepared at various concentrations for optimal staining of different tissue types. Tissue samples were stained for 1 minute, before washing in 1X PBS twice, 30 seconds each. Samples were blotted dry with Kimwipes and placed on modified histology cassettes for imaging. 0.1 mg/mL Hoechst with 2 mg/mL Rhodamine B was identified as an effective fluorescent concoction for general staining over a wide range of murine tissues from fresh and fixed renal systems, to the heart, and the digestive and female reproductive tract. 0.1 mg/mL Hoechst with 4 mg/mL Rhodamine B was also used to more strongly contrast the structural features of organs such as the tubules of fresh kidneys. Organs which featured a high level of nuclear concentration such as the ovaries and gastric surface of the stomach were better highlighted with a lower level of nuclear stain ratio of 0.1 mg/mL Hoechst with 1 mg/mL Rhodamine B and 0.05 mg/mL Hoechst with 2 mg/mL Rhodamine B respectively.

Viability studies For cell viability experiments, 1 x 10^6 cells/mL MCF-7 cells were seeded onto modified 6-well plates. Prior to imaging, media was removed and cells were stained with a total of 750 μL of viability stains 1:1 SYTO 9 and propidium iodide nucleic acid stain (1.5 μL SYTO 9 to 1.5 μL PI per 1 mL PBS) for 15 minutes (L7007, LIVE/DEAD™ BacLight™ Bacterial Viability Kit, for microscopy, Invitrogen). At the point of imaging, 250 μL of 70% ethanol was added to induce cell death. Images of cells were acquired every minute over 60 minutes. For visualisation of tissue viability, samples were incubated in 7:1 SYTO 9 and propidium iodide nucleic acid stain (7.5 μL SYTO 9 to 1.5 μL propidium iodide per 1 mL PBS) for 15 minutes. Samples were blotted dry with Kimwipes and placed on modified histology cassettes for imaging. For kidney viability studies, slices (700 μm) were treated with antibiotic insult vancomycin (vancomycin hydrochloride hydrate, 861987, Sigma Aldrich) (5 mg/mL or 10 mg/mL) for 1 hour with PBS as control. After treatment, sections were washed in PBS. Kidney tissue was stained similarly as above with viability stains. Methods were illustrated in Fig 5g, created with BioRender.com.

Viability comparisons for renal corpuscles and proximal tubules were done by the cropping of regions of interest before quantification. Cortex and medullas were manually cropped using ImageJ for each of the 18 kidney samples. 20 longitudinal proximal tubules were manually cropped from each kidney sample due to their non-uniform shape. All renal corpuscles were semi-automatically cropped by first dotting any visible corpuscle structure using Paint then using a custom Python script to detect the dots and cropping a constant window around each dot. Over 2,000 crops were generated using this method. Viability was compared between treatment groups and tissue structure and results were expressed as the ± standard error of the mean (SEM). OriginLab was used for graph plotting and analysis.

Viability quantification Image-based viability quantification was estimated by computing the proportion of image pixels that represent live cells. Viability stains SYTO 9 and propidium iodide primarily fluoresce green

and red respectively. Hence, the green and red channels of the image were used to estimate the fluorescent signals from live and dead cells respectively. Since propidium iodide is only permeable to dead cells and replaces SYTO 9, the point where the red signal is greater than the green distinguishes dead cells from live ones. Propidium iodide exhibits a stronger affinity for nucleic acids than SYTO 9 and thus displaces SYTO 9 in dead cells [50]. The proportion of pixels representing dead cells (and conversely live cells) was computed to estimate the percentage viability of the sample. Both images of single-cell samples, as well as tissue samples, went through background removal using Otsu's method on grey-scale versions of said images prior to viability quantification.

Immunohistochemistry Mouse uterus cross-section tissue (1 mm) were fixed for 30 minutes in 4% formaldehyde (VWR) before blocking and permeabilisation for 2 hours in 1% BSA (W384A, Promega) and 0.5% Triton-X (H5141, Promega) for 2 hours. Thereafter, primary antibodies 1/100 Anti-Fibronectin (ab2413, Abcam) and Anti-Laminin (ab2466, Abcam) were added to the uterus slices and incubated for 16 hours. The slices were washed twice in 1X PBS, 5 minutes each, before secondary antibodies 1/100 Alexa-Fluor 594 (ab150160, Abcam) and Alexa-Fluor 488 (A11034, Life Technologies) were applied and left to incubate 5 hours. After incubation, samples were washed twice in 1X PBS for 5 minutes prior to imaging.

5.3 Image acquisition and large-field mosaicing

Imaging setting and processing Colour images were captured with exposure ranging between 0.1 to 3 seconds. The gain was typically set at 15. Both the red and blue gain ratio was usually set between 1.5 and 2.4. The images were saved in PNG file format. Image processing was done with the open-source ImageJ (Fiji) [51] and limited to adjustments of brightness and contrast, colour balance, and the occasional despeckling to remove hot pixels.

Automated image acquisition Image acquisition was facilitated by the integration of C code on the Arduino, Python code on a laptop attached to the microscope, and the Teledyne FLIR Spinnaker SDK. Manual image acquisition was done using an analogue stick with the Arduino for motor control and the SpinView GUI from the Spinnaker SDK for the viewing and saving of images. Automated image acquisition for large mosaic images was coordinated by our custom Python software. It received and processed user input, then controlled the camera through the Python API from the Spinnaker SDK and the stage by sending condensed instructions to the Arduino.

Large-field mosaicing Large-field mosaicing was enabled by the Python software integrated with the microscope and the freely available Microsoft Image Composite Editor. Images were automatically and sequentially captured with an adjustable overlap (usually 15% margins) and stitched together using Image Composite Editor to achieve gigapixel-sized mosaic images comprising hundreds of individual images. The sample stage was precise enough for images to be manually focused prior to imaging, with the Python software subsequently automatically controlling the movement and capture of images, without additional refocusing required, over the entire sample area.

5.4 3D microtopography with photometric stereo

Sequential illumination for microtopography To obtain the micro-topographical information over a region of interest on a sample, each of the fibre optics was coupled to an independently controlled DUV LED. A reference image of the region of interest was then captured with illumination coming from all the fibre optics. Sequential images with directional illumination from each of the fibre optics were then obtained while maintaining the same field of view over the region of interest. The exposure of the sequential images was increased compared to the reference image, to compensate for the dimmer illumination coming from a single fibre optic. Despeckling was performed on all images using ImageJ to remove hot pixels. Following this, the sequential images were histogram matched with the reference image to obtain the different direction-of-illumination images with the same relative brightness. The unique images of the region of interest, along with a generic representative vector for each direction of fibre optic illumination, were then inputted into our implementation of the classic photometric stereo algorithm (vectorised and ported to Python based on Zhang [52]) to obtain the surface normals and depth map of the region of interest. Finally, the depth map was rendered in 3D, with the despeckled reference image used as the surface texture in PyVista, to produce an interactive 3D micro-topographical reconstruction of the sample region of interest.

Isotropic response of fluorescent samples The DUV fluorescence microscope presented here is well suited to exploit the photometric stereo method, first introduced by Robert Woodham in 1980 [20], to obtain 3D surface microtopographical features. With Woodham's original assumptions, a Lambertian surface which perfectly diffuses reflection is required. This is unrealistic for most real-life materials and use cases, which are non-Lambertian and anisotropic, which has led to multiple various methods being developed to relax this requirement [53, 54]. The isotropic response [46] of fluorescently stained biological samples, in this case, is ideal. Since fluorescence emissions radiate isotropically with ideal Lambertian characteristics [45, 55], errors associated with reflected light are avoided, capturing a better and more accurate estimation of the 3D microtopography.

Classic Photometric Stereo The classic photometric stereo method is described [56] by each pixel as, the luminous intensity (I) or apparent brightness being determined by the surface irradiance (I_0), the cosine of the angle between the unit vector of the direction of the illumination source ($\hat{s}$) and unit vector of the surface normal ($\hat{n}$), and the albedo or reflection coefficient as a constant factor (A).

$$I = A.I_0.\hat{s}.\hat{n}$$

With no specular reflections and cast shadows from the Lambertian fluorescent sample, each pixel is represented as,

$$m_i = \hat{s}_i.\vec{n}$$

where (i) is the light source coming from the vector direction ($\hat{s}_i$), with an intensity of (m_i), where $\vec{n} = [n_x, n_y, n_z]^T$ is a unitless vector of magnitude ($A.I_0$) and direction ($\hat{n}$). A sequence of 3 measurements can thus be expressed as,

$$\begin{bmatrix} S_x1 & S_y1 & S_z1 \\ S_x2 & S_y2 & S_z2 \\ S_x3 & S_y3 & S_z3 \end{bmatrix} \begin{bmatrix} n_x \\ n_y \\ n_z \end{bmatrix} = \begin{bmatrix} m_1 \\ m_2 \\ m_3 \end{bmatrix}$$

If the sample and the illumination sources are not on the same plane, and the illumination source matrix is non-singular, the linear equations system can be solved for $\vec{n}$. For cases where there are more than 3 measurements, an estimation of the normal vector $\vec{n}$ can be made by minimising the residual error with the source vector, $\arg\min_{n_x,n_y,n_z} \sqrt{\sum_i (\hat{s}_i.\vec{n} - m_i)^2}$ Essentially, the overdetermined system of linear equations represents every pixel's intensity being proportionate to the dot product of the illumination vector and the surface normal. Thus, this allows the surface normals of every pixel of the sample to be obtained. The surface normals can be further interpreted with geometrical arguments to produce an approximate depth map.

6 Bibliography

References

1. Bhatia, H. S. *et al.* Spatial proteomics in three-dimensional intact specimens. *Cell* **185.** Publisher: Elsevier, 5040–5058.e19 (Dec. 22, 2022).
2. Rao, A., Barkley, D., França, G. S. & Yanai, I. Exploring tissue architecture using spatial transcriptomics. *Nature* **596.** Number: 7871 Publisher: Nature Publishing Group, 211–220 (Aug. 2021).
3. Voskuil, F. J. *et al.* Intraoperative imaging in pathology-assisted surgery. *Nature Biomedical Engineering* **6.** Number: 5 Publisher: Nature Publishing Group, 503–514 (May 2022).
4. Lemon, W. C. & McDole, K. Live-cell imaging in the era of too many microscopes. *Current Opinion in Cell Biology. Cell Dynamics* **66,** 34–42 (Oct. 1, 2020).
5. Gibbs, S. L. *et al.* Near-Infrared Fluorescent Digital Pathology for the Automation of Disease Diagnosis and Biomarker Assessment. *Molecular Imaging* **14,** 7290.2015.00005 (May 2015).
6. Li, Y. *et al.* Hematoxylin and eosin staining of intact tissues via delipidation and ultrasound. *Scientific Reports* **8,** 12259 (Aug. 16, 2018).
7. Wang, J., Xu, Y. & Boppart, S. A. Review of optical coherence tomography in oncology. *Journal of Biomedical Optics* **22,** 1–23 (Dec. 2017).
8. Ming, Y. *et al.* Longitudinal morphological and functional characterization of human heart organoids using optical coherence tomography. *Biosensors & Bioelectronics* **207,** 114136 (July 1, 2022).
9. Costa, P. C. *et al.* Towards in-vivo label-free detection of brain tumor margins with epi-illumination tomographic quantitative phase imaging. *Biomedical Optics Express* **12.** Publisher: Optica Publishing Group, 1621–1634 (Mar. 1, 2021).

10. Ragazzi, M. *et al.* Fluorescence confocal microscopy for pathologists. *Modern Pathology* **27.** Number: 3 Publisher: Nature Publishing Group, 460–471 (Mar. 2014).

11. Tao, Y. K. *et al.* Assessment of breast pathologies using nonlinear microscopy. *Proceedings of the National Academy of Sciences of the United States of America* **111,** 15304–15309 (Oct. 28, 2014).

12. Mertz, J. Optical sectioning microscopy with planar or structured illumination. *Nature Methods* **8.** Number: 10 Publisher: Nature Publishing Group, 811–819 (Oct. 2011).

13. Zhang, Y., Kang, L., Lo, C. T. K., Tsang, V. T. C. & Wong, T. T. W. Rapid slide-free and non-destructive histological imaging using wide-field optical-sectioning microscopy. *Biomedical Optics Express* **13.** Publisher: Optica Publishing Group, 2782–2796 (May 1, 2022).

14. Lin, B., Urayama, S., Saroufeem, R. M. G., Matthews, D. L. & Demos, S. G. Real-time microscopic imaging of esophageal epithelial disease with autofluorescence under ultraviolet excitation. *Optics Express* **17.** Publisher: Optica Publishing Group, 12502–12509 (July 20, 2009).

15. Fereidouni, F. *et al.* Microscopy with ultraviolet surface excitation for rapid slide-free histology. *Nature Biomedical Engineering* **1.** Number: 12 Publisher: Nature Publishing Group, 957–966 (Dec. 2017).

16. Yoshitake, T. *et al.* Rapid histopathological imaging of skin and breast cancer surgical specimens using immersion microscopy with ultraviolet surface excitation. *Scientific Reports* **8.** Number: 1 Publisher: Nature Publishing Group, 4476 (Mar. 14, 2018).

17. Xie, W. *et al.* Microscopy with ultraviolet surface excitation for wide-area pathology of breast surgical margins. *Journal of Biomedical Optics* **24,** 026501 (Feb. 2019).

18. Guo, J., Artur, C., Womack, T., Eriksen, J. L. & Mayerich, D. Multiplex protein-specific microscopy with ultraviolet surface excitation. *Biomedical Optics Express* **11.** Publisher: Optica Publishing Group, 99–108 (Jan. 1, 2020).

19. Liu, Y., Rollins, A. M., Levenson, R. M., Fereidouni, F. & Jenkins, M. W. Pocket MUSE: an affordable, versatile and high-performance fluorescence microscope using a smartphone. *Communications Biology* **4.** Number: 1 Publisher: Nature Publishing Group, 1–14 (Mar. 12, 2021).

20. Woodham, R. Photometric method for determining surface orientation from multiple images. *Optical Engineering* **19,** 139–144 (Jan. 1, 1980).

21. Qorbani, A. *et al.* Microscopy with ultraviolet surface excitation (MUSE): A novel approach to real-time inexpensive slide-free dermatopathology. *Journal of Cutaneous Pathology* **45.** _eprint: https://onlinelibrary.wiley.com/doi/ 498–503 (2018).

22. Arimura, Y. *et al.* Mitochondrial superoxide production contributes to vancomycin-induced renal tubular cell apoptosis. *Free Radical Biology and Medicine* **52,** 1865–1873 (May 2012).

23. Braun, J. *et al.* Toxic Effect of Vancomycin on Viability and Functionality of Different Cells Involved in Tissue Regeneration. *Antibiotics* **9,** 238 (May 8, 2020).

24. Bariteau, J. T., Kadakia, R. J., Traub, B. C., Viggeswarapu, M. & Willett, N. J. Impact of Vancomycin Treatment on Human Mesenchymal Stromal Cells During Osteogenic Differentiation (2018).

25. *LIVE/DEAD BacLight Bacterial Viability Kits* `https://www.thermofisher.com/order/catalog/product/l7007`.

26. Giacomelli, M. G. *et al.* Virtual Hematoxylin and Eosin Transillumination Microscopy Using Epi-Fluorescence Imaging. *PLOS ONE* **11.** Publisher: Public Library of Science, e0159337 (Aug. 8, 2016).

27. Serafin, R., Xie, W., Glaser, A. K. & Liu, J. T. C. FalseColor-Python: A rapid intensity-leveling and digital-staining package for fluorescence-based slide-free digital pathology. *PLOS ONE* **15.** Publisher: Public Library of Science, e0233198 (Oct. 1, 2020).

28. Rodvold, K. A. *et al.* Vancomycin pharmacokinetics in patients with various degrees of renal function. *Antimicrobial Agents and Chemotherapy* **32,** 848–852 (June 1988).

29. Dieterich, C. *et al.* Gene expression analysis reveals new possible mechanisms of vancomycin-induced nephrotoxicity and identifies gene markers candidates. *Toxicological Sciences: An Official Journal of the Society of Toxicology* **107,** 258–269 (Jan. 2009).

30. Pais, G. M. *et al.* Vancomycin-Induced Kidney Injury: Animal Models of Toxicodynamics, Mechanisms of Injury, Human Translation, and Potential Strategies for Prevention. *Pharmacotherapy: The Journal of Human Pharmacology and Drug Therapy* **40,** 438–454 (May 2020).

31. Rose, W., Volk, C., Dilworth, T. J. & Sakoulas, G. Approaching 65 Years: Is It Time to Consider Retirement of Vancomycin for Treating Methicillin-Resistant Staphylococcus aureus Endovascular Infections? *Open Forum Infectious Diseases* **9,** ofac137 (May 2022).

32. Bamgbola, O. Review of vancomycin-induced renal toxicity: an update. *Therapeutic Advances in Endocrinology and Metabolism* **7,** 136–147 (June 2016).

33. Luque, Y. *et al.* Vancomycin-Associated Cast Nephropathy. *Journal of the American Society of Nephrology* **28,** 1723–1728 (June 2017).

34. Giehl, N., Nobakht, N., Kamgar, M. & Zuckerman, J. Minimizing Vancomycin-Associated Acute Interstitial Nephritis (2022).

35. Crawford, C. *et al.* An Intact Kidney Slice Model to Investigate Vasa Recta Properties and Function in situ. *Nephron Physiology* **120,** p17–p31 (July 20, 2012).

36. Humanes, B. *et al.* Protective Effects of Cilastatin against Vancomycin-Induced Nephrotoxicity. *BioMed Research International* **2015,** 704382 (2015).

37. Pais, G. M. *et al.* Lack of synergistic nephrotoxicity between vancomycin and piperacillin/tazobactam in a rat model and a confirmatory cellular model. *Journal of Antimicrobial Chemotherapy* **75,** 1228–1236 (May 1, 2020).

38. Yu, P. *et al.* N-acetylcysteine Ameliorates Vancomycin-induced Nephrotoxicity by Inhibiting Oxidative Stress and Apoptosis in the in vivo and in vitro Models. *International Journal of Medical Sciences* **19,** 740–752 (2022).

39. Khalili, H., Bairami, S. & Kargar, M. Antibiotics induced acute kidney injury: incidence, risk factors, onset time and outcome. *Acta Medica Iranica* **51,** 871–878 (2013).

40. Zamoner, W., Prado, I. R. S., Balbi, A. L. & Ponce, D. Vancomycin dosing, monitoring and toxicity: Critical review of the clinical practice. *Clinical and Experimental Pharmacology and Physiology* **46,** 292–301 (Apr. 2019).

41. He, J. *et al.* Vitamin C reduces vancomycin-related nephrotoxicity through the inhibition of oxidative stress, apoptosis, and inflammation in mice. *Annals of Translational Medicine* **9,** 1319–1319 (Aug. 2021).

42. Im, D. s. *et al.* Cilastatin attenuates vancomycin-induced nephrotoxicity via P-glycoprotein. *Toxicology Letters* **277,** 9–17 (Aug. 2017).

43. Kandemir, F. M. *et al.* Therapeutic efficacy of zingerone against vancomycin-induced oxidative stress, inflammation, apoptosis and aquaporin 1 permeability in rat kidney. *Biomedicine & Pharmacotherapy* **105,** 981–991 (Sept. 2018).

44. Ching-Roa, V. D., Huang, C. Z. & Giacomelli, M. G. Improved microscopy with ultraviolet surface excitation (MUSE) using high-index immersion illumination. *Biomedical Optics Express* **12,** 6461–6473 (Sept. 22, 2021).

45. Treibitz, T., Murez, Z., Mitchell, B. G. & Kriegman, D. *Shape from Fluorescence* in *Computer Vision – ECCV 2012* European Conference on Computer Vision (Springer, Berlin, Heidelberg, 2012), 292–306.

46. Salvant, J. *et al. Photometric Stereo by UV-Induced Fluorescence to Detect Protrusions on Georgia O'Keeffe's Paintings* Nov. 21, 2017.

47. Davnall, F. *et al.* Assessment of tumor heterogeneity: an emerging imaging tool for clinical practice? *Insights into Imaging* **3,** 573–589 (Oct. 24, 2012).

48. Bashir, U., Siddique, M. M., Mclean, E., Goh, V. & Cook, G. J. Imaging Heterogeneity in Lung Cancer: Techniques, Applications, and Challenges. *AJR. American journal of roentgenology* **207,** 534–543 (Sept. 2016).

49. Smith, B. H. & Edward Berk, J. The detection of upper gastrointestinal bleeding sites by ultraviolet endoscopy. *Gastrointestinal Endoscopy* **19,** 123–124 (Feb. 1, 1973).

50. Stiefel, P., Schmidt-Emrich, S., Maniura-Weber, K. & Ren, Q. Critical aspects of using bacterial cell viability assays with the fluorophores SYTO9 and propidium iodide. *BMC Microbiology* **15,** 36 (Dec. 2015).

51. Schindelin, J. *et al.* Fiji: an open-source platform for biological-image analysis. *Nature Methods* **9.** Number: 7 Publisher: Nature Publishing Group, 676–682 (July 2012).

52. Zhang, X. *photometric-stereo* original-date: 2015-04-19T14:36:39Z. Dec. 19, 2022.

53. Collins, T. & Bartoli, A. in *Medical Image Computing and Computer-Assisted Intervention – MICCAI 2012* (eds Ayache, N., Delingette, H., Golland, P. & Mori, K.) red. by Hutchison, D. *et al.* Series Title: Lecture Notes in Computer Science, 634–642 (Springer Berlin Heidelberg, 2012). ISBN: 978-3-642-33417-7 978-3-642-33418-4.

54. Ackermann, J. & Goesele, M. A Survey of Photometric Stereo Techniques. *Foundations and Trends® in Computer Graphics and Vision* **9,** 149–254 (2015).

55. Lu, F., Matsushita, Y., Sato, I., Okabe, T. & Sato, Y. From Intensity Profile to Surface Normal: Photometric Stereo for Unknown Light Sources and Isotropic Reflectances. *IEEE transactions on pattern analysis and machine intelligence* **37,** 1999–2012 (Oct. 2015).

56. Parot, V. *et al.* Photometric stereo endoscopy. *Journal of Biomedical Optics* **18,** 076017 (July 2013).

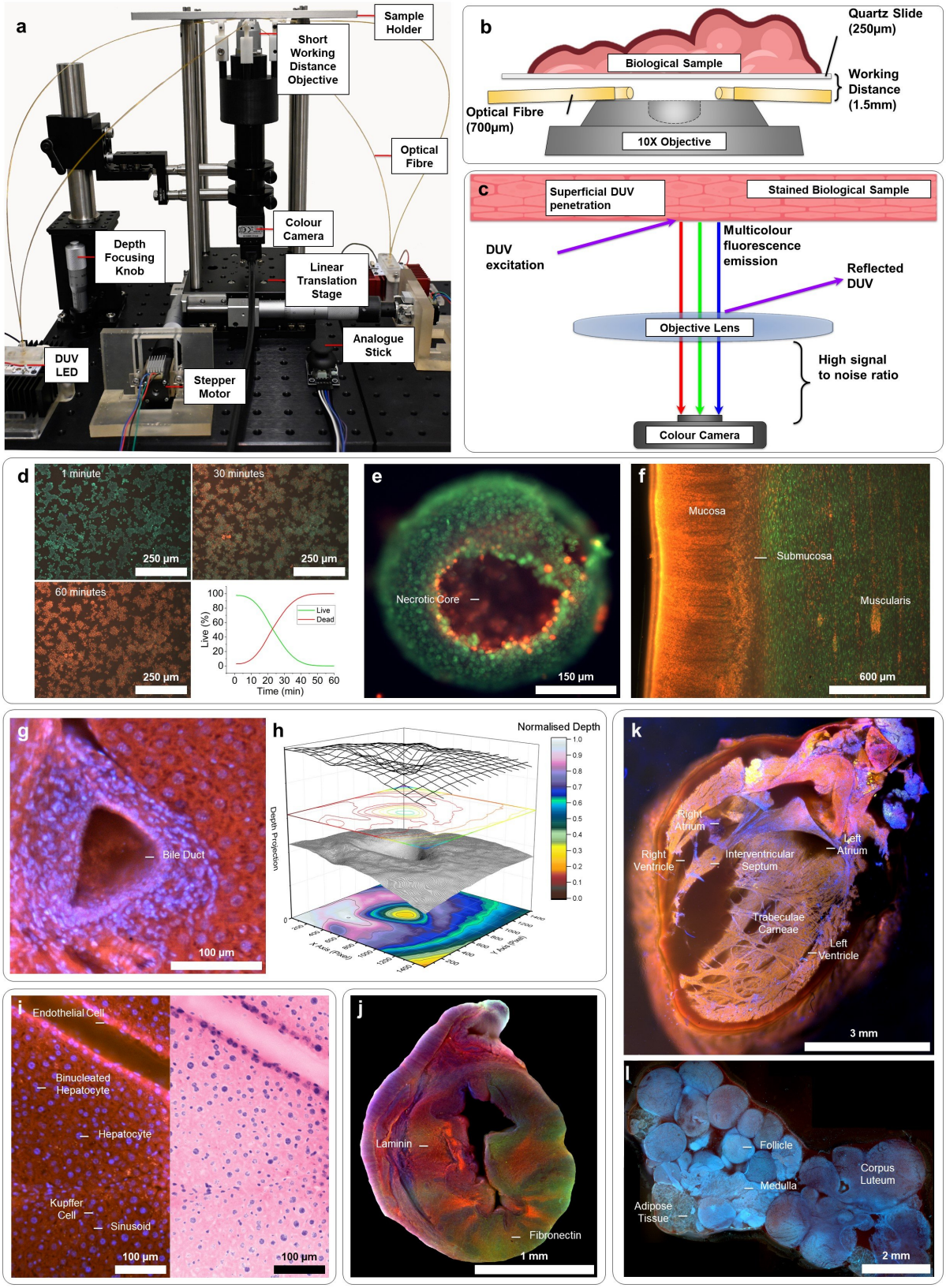

Figure 1: Overview of microscope and capabilities. a. Key components of the microscope. Optical fibres carry DUV light from LEDs to the sample. b. Multimode fibres allow for oblique epi-illumination via very short working distances. c. DUV superficially excites the surface of stained biological tissue and produces multicolour fluorescence emissions. The glass objective excludes DUV, resulting in images with a high signal-to-noise ratio. d. Quantification of single cell (MCF-7) percentage viability over time after exposure to chemical insults. e. Spheroid (MCF-7) imaging showed a red necrotic core contrasting starkly with the green proliferative layer. f. Viability staining can highlight tissue structure despite primarily staining cell nuclei. The mucosa, submucosa and muscularis mucosa of fresh mouse stomach is clearly differentiated by their viability. g-h. Fluorescence image and 3D reconstruction of formalin-fixed mouse liver. A strong quasi-3D effect is observed, with the highly nucleated bile duct extending deeper and beyond focus into the tissue. 3D reconstruction was obtained using photometric stereo. i. Fluorescence image (left) of formalin-fixed mouse liver with the corresponding virtual H&E recoloured image (right). Hepatocytes and sinusoids are distinguishable. The flat nuclei of endothelial cells are also seen lining the vein. j. Multiplexed image of fixed mouse uterus with immunohistochemical staining for fibronectin (green) and laminin (red) of the extracellular matrix. The faint blue signal originates from the autofluorescence of the fixed tissue. k. Large field-of-view mosaics enable whole organ visualisation of a fresh mouse heart at 4X magnification and millimetre scale. The coronal section displays the 4 main chambers and architectural organisation of the trabeculae carneae on the endocardial surface with a quasi-3D perspective. l. Freshly excised rat ovary reveals a clear distinction between follicles at different developmental stages and associated features of the ovary.

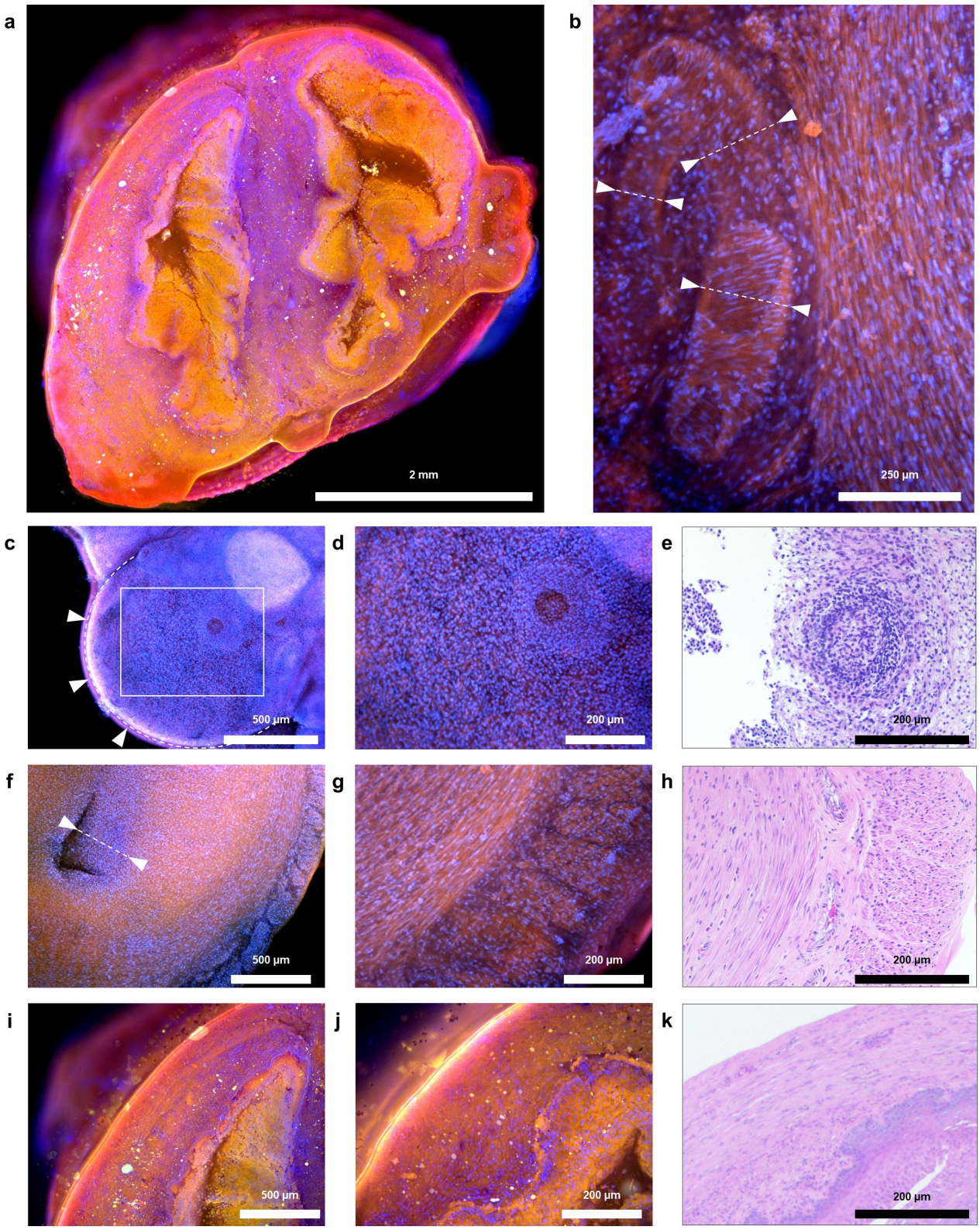

Figure 2: The female reproductive tract. a. Cut surface of a fresh rat cervix that reveals the merging of two uterine horns distal to the uterine junction. The inner surface of the endometrium is visibly textured. b. Three interlacing blood vessels located in the stratum vasculare of fresh rat uterus at 10X magnification. The vessels have an approximate diameter of 140 μm, 130 μm, and 75 μm with a wall thickness of 25 μm, 25 μm and 18 μm respectively. c-e. 4X and 10X images and H&E histology of the intact surface of a fresh rat ovary, with a developing secondary follicle, is identified by the multi-cell thickness at the edge of the follicle and a measured diameter of 1160 μm. At a higher magnification, the granulosa layer is distinct with clear visualisation of the oocyte eccentrically positioned. f-h. 4X and 10X images and H&E histology of the cut surface of a fresh rat uterus, with all three layers (perimetrium, myometrium, endometrium) of the uterus clearly visible and distinguishable from each other. The uterus has a measured radius of approximately 1410 μm with the stratum functionalis being roughly 350 µm thick, measurements that could be used in aiding the staging of the estrus cycle. At higher magnification, the inner circular layer of smooth muscles transitions to the outer longitudinal layer of smooth muscles in the myometrium, separated by stratum vasculare. i-k. 4X, and 10X images and H&E histology of fresh rat cervix, lumen of a single uterine horn.

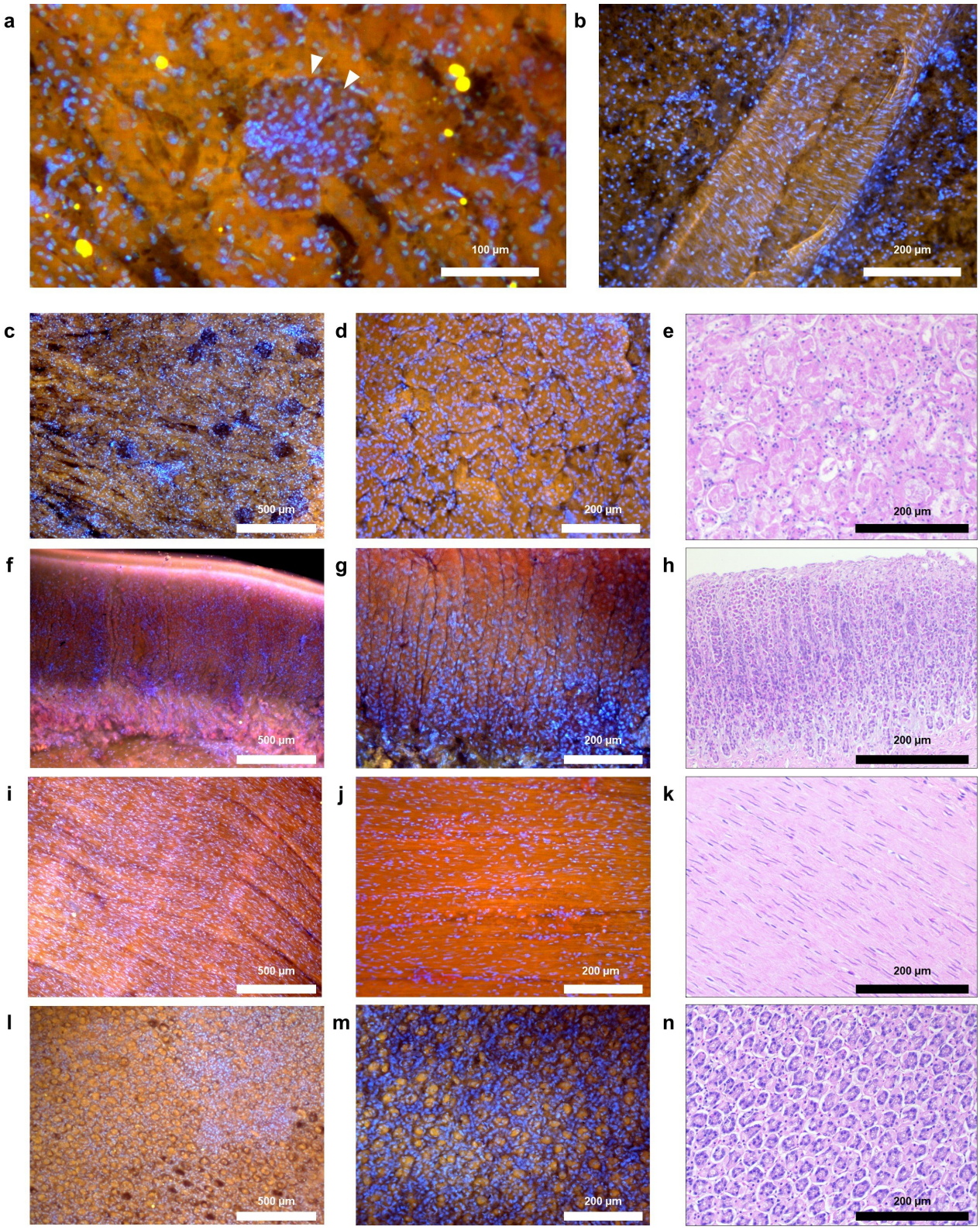

Figure 3: The kidney and stomach. a. Renal glomerulus in fresh mouse kidney, note epithelial parietal cells (white arrows) of Bowman's capsule. b. Partially cut surface of a large blood vessel in fresh mouse kidney, revealing the inner surface of a blood vessel. c. Kidney cortex of a fresh mouse kidney, showing multiple renal corpuscles at 4X magnification. d. *Enface* surface of fresh mouse renal tubules at 10X magnification. e. Corresponding H&E of the same sample, renal tubules. f-h. 4X and 10X images and H&E histology of fresh rat stomach mucosa. i-k. 4X and 10X images and H&E histology of smooth muscle of a fresh rat's outer stomach. l-n. 4X and 10X images and H&E histology of gastric pits on an inner surface of a fresh rat stomach. Higher magnification reveals surface mucous cells forming the gastric openings.

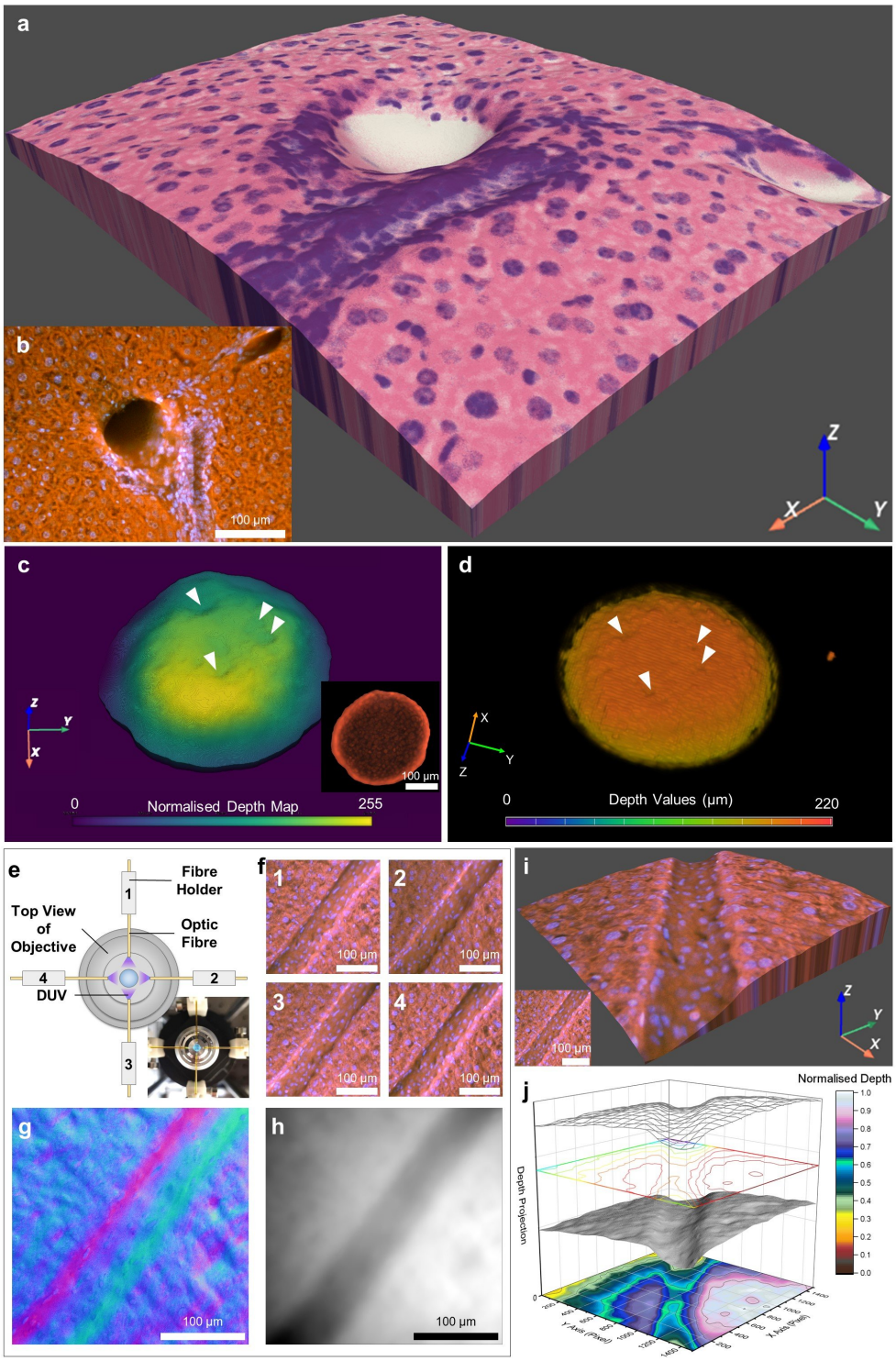

Figure 4: Microtopography. a. 3D virtual H&E recoloured render of fixed mouse liver showing a vein stretching distally into the tissue, with a smaller highly nucleated bile duct running vertically. Further right, a venule, likely feeding to the vein, extends further into the tissue. b. Fluorescence image of the same region of interest. c. The 3D render presents the normalised depth map of a fixed spheroid (MCF-7) stained with propidium iodide. d. The same spheroid was imaged on a confocal microscope to obtain the depth map of the spheroid. e. Top-down schematic view of the microscope objective. f. Images obtained by sequentially illuminating a longitudinally cut blood vessel in a fixed mouse liver and histogram matched to a reference image with multi-directional illumination from all 4 fibres. g. The surface normal vector map is obtained through the photometric stereo algorithm, revealing the liver surface direction, edge, and shape of the blood vessel. h. The depth map is obtained from the surface normal map, highlighting the concaved inner wall of the blood vessel. i. 3D render of the blood vessel is shown with the multi-directional illuminated image as the surface texture of the 3D model, allowing a greater appreciation of the 3D physical characteristics of the blood vessel and surface texture. j. 3D reconstructed normalised depth projection of the region of interest is shown, highlighting the 3D depth contours.

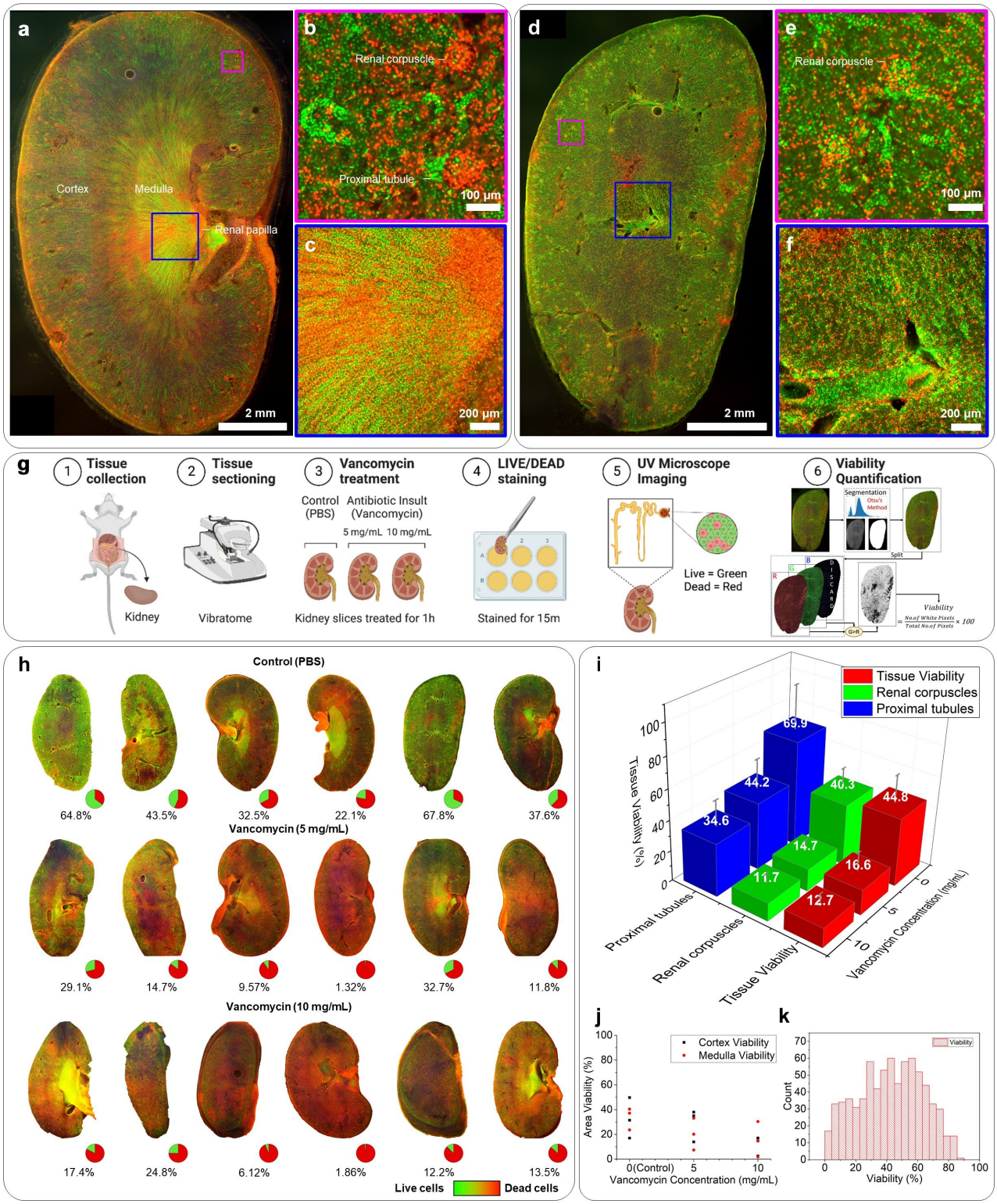

Figure 5: Tissue viability studies. Longitudinally-sectioned mouse kidney exposed to (a) antibiotic vancomycin insult 5 mg/mL and (d) control PBS for 1 hour and subsequently stained with viability assay. b. Part of nephron with visible renal corpuscle extending to the proximal convoluted tubule. c. Papilla at the apex of the renal pyramid, transitioning from collecting ducts (left) into papillary ducts (right). e. Renal corpuscles with capillary loops of glomerulus. f. Longitudinal view of renal blood vessels with distinctive epithelial cell morphology and lumen. g. Kidney viability insult experiment methodology. h. Stitched images of all kidney slices. Rows show control (PBS), vancomycin 5 mg/mL and 10 mg/mL respectively. Pie charts represent the whole tissue viability. Control tissue show an overall lower proportion of propidium iodide staining than that of the vancomycin-treated tissues. i. Data plots highlight the decrease in viability with increasing vancomycin concentrations. A comparison of the viability in whole tissue (n=18), renal corpuscles (n=2084) and proximal convoluted tubules (n=180) was performed. j. Comparison of viability in the cortex vs medulla of all kidney slices. k. Distribution of control renal corpuscles (n=752) viability, showing inter-tissue and intra-tissue variability. All images were acquired at 4X magnification using our microscope.

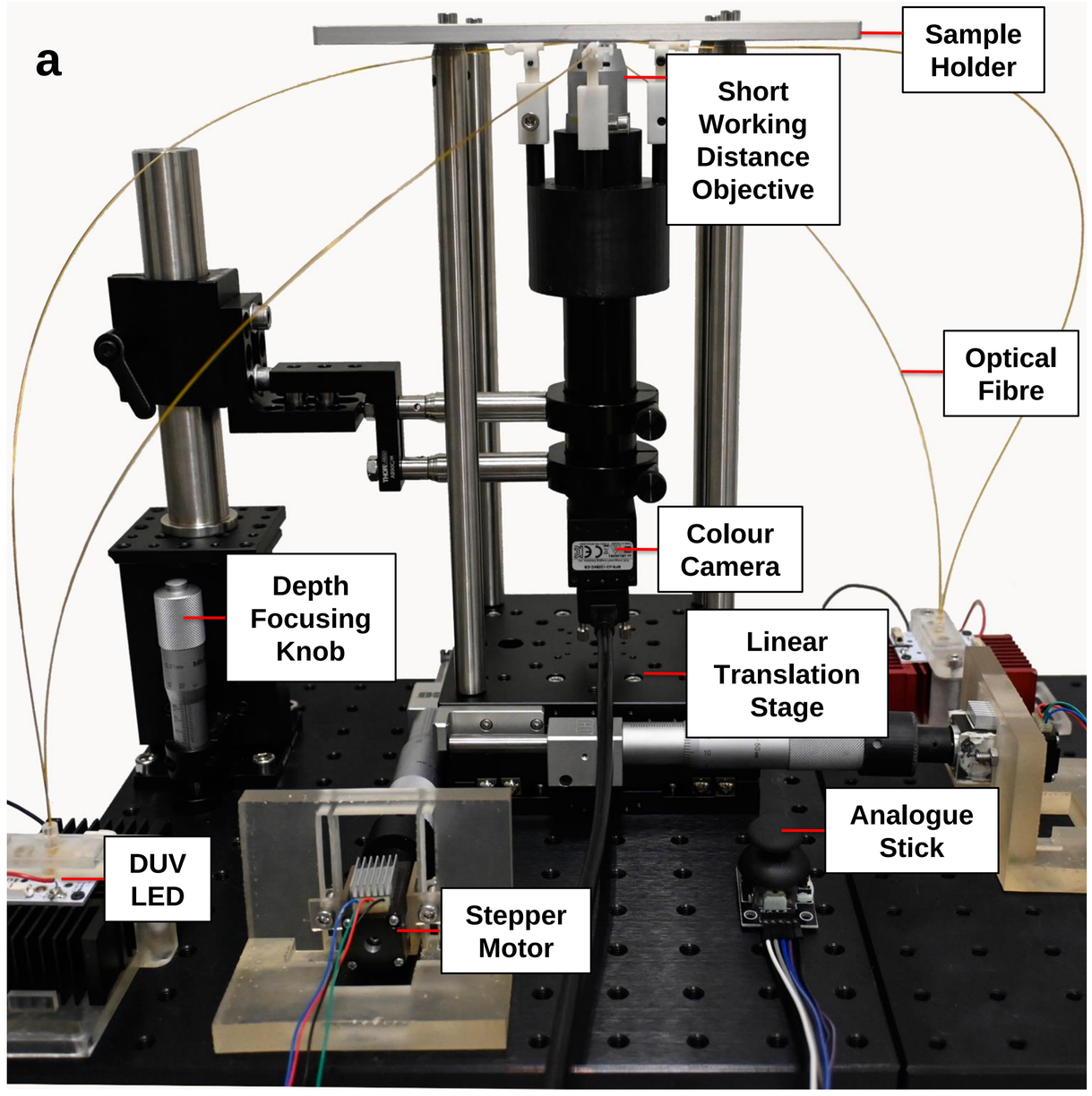
a
Sample Holder
Short Working Distance Objective
Optical Fibre
Colour Camera
Depth Focusing Knob
Linear Translation Stage
Analogue Stick
DUV LED
Stepper Motor

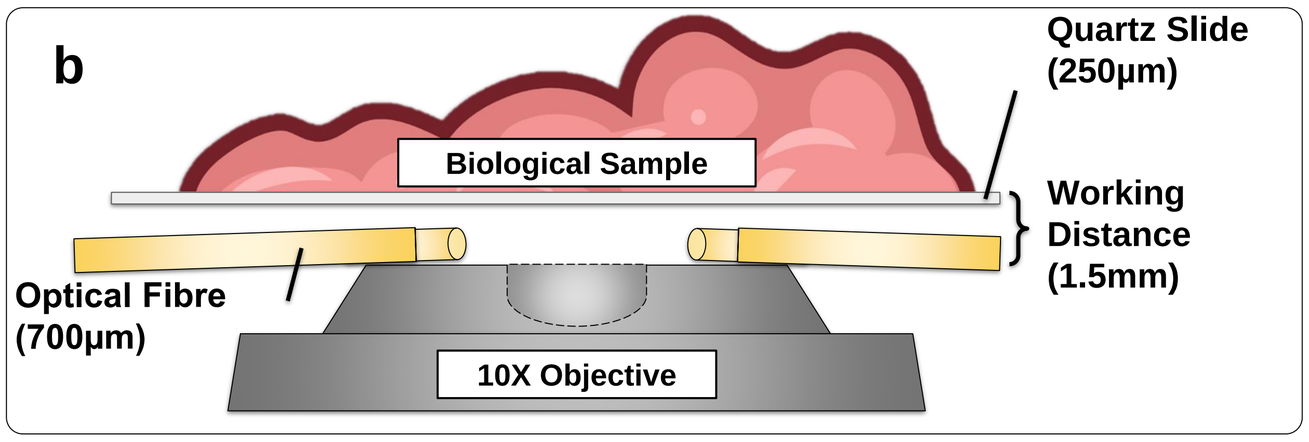
b
Quartz Slide (250µm)
Biological Sample
Working Distance (1.5mm)
Optical Fibre (700µm)
10X Objective

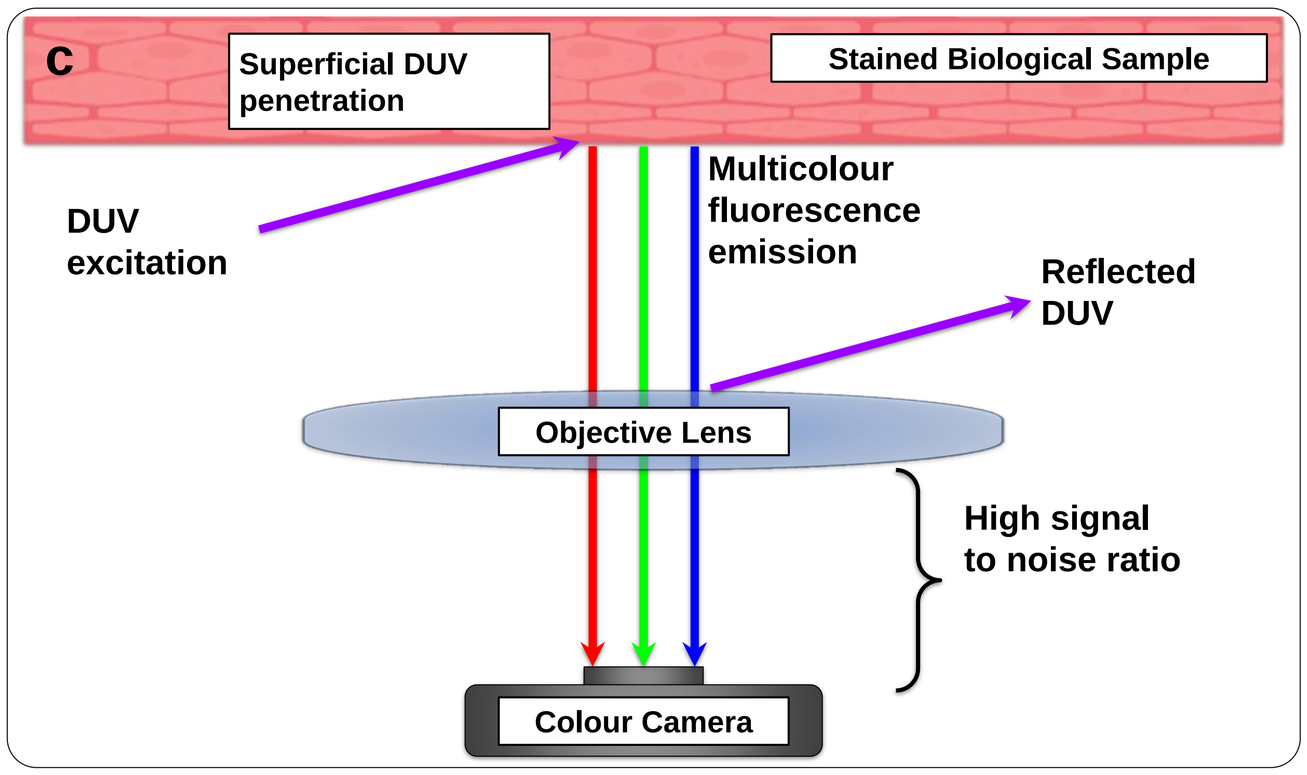
c
Superficial DUV penetration
Stained Biological Sample
DUV excitation
Multicolour fluorescence emission
Reflected DUV
Objective Lens
High signal to noise ratio
Colour Camera

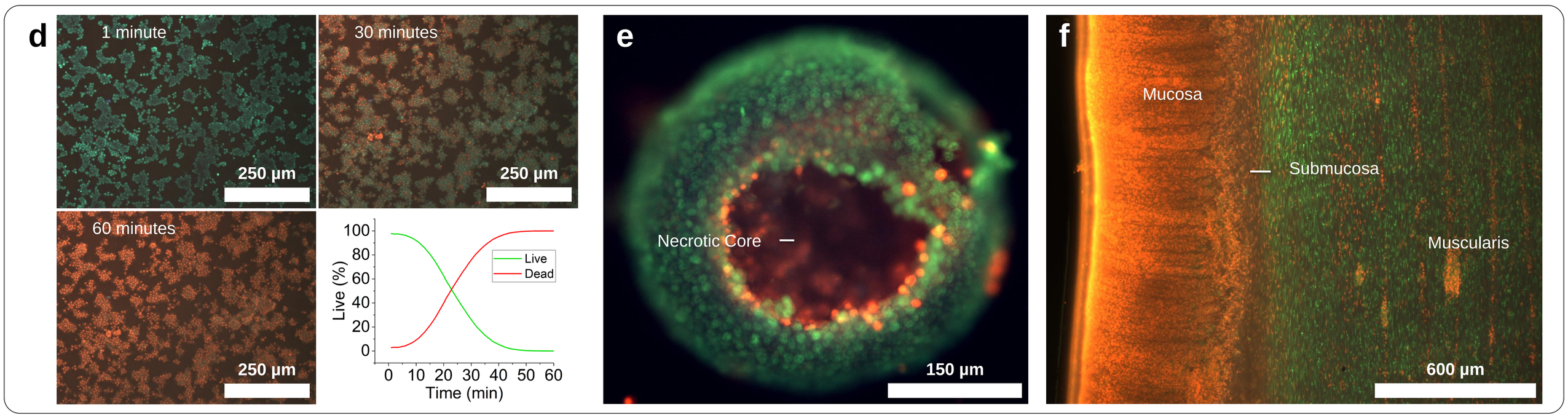
d
1 minute
30 minutes
60 minutes
250 µm
Live (%)
Time (min)
Live
Dead
e
Necrotic Core
150 µm
f
Mucosa
Submucosa
Muscularis
600 µm

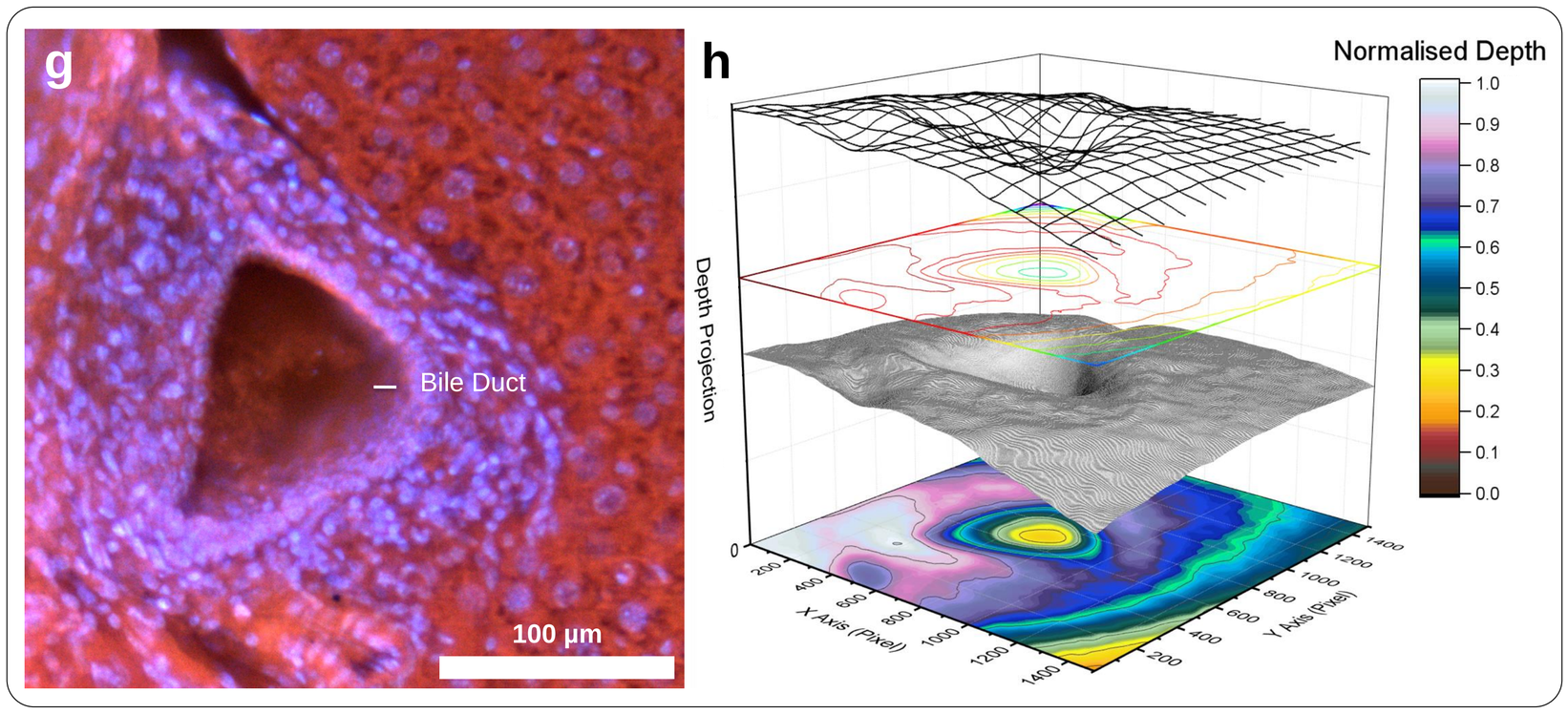
g
Bile Duct
100 µm
h
Normalised Depth
Depth Projection
X Axis (Pixel)
Y Axis (Pixel)

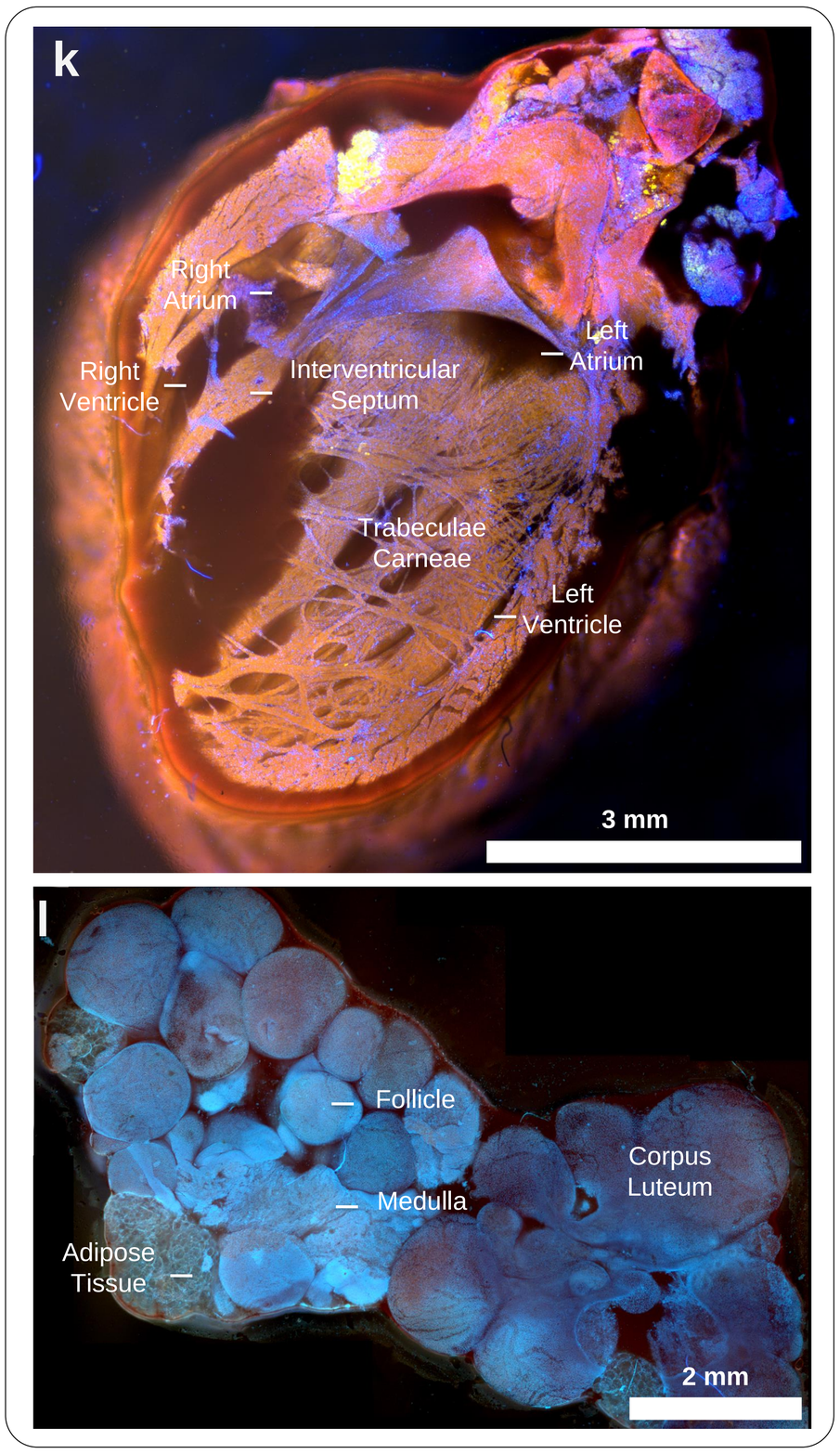
k
Right Atrium
Right Ventricle
Interventricular Septum
Left Atrium
Trabeculae Carneae
Left Ventricle
3 mm
l
Follicle
Medulla
Corpus Luteum
Adipose Tissue
2 mm

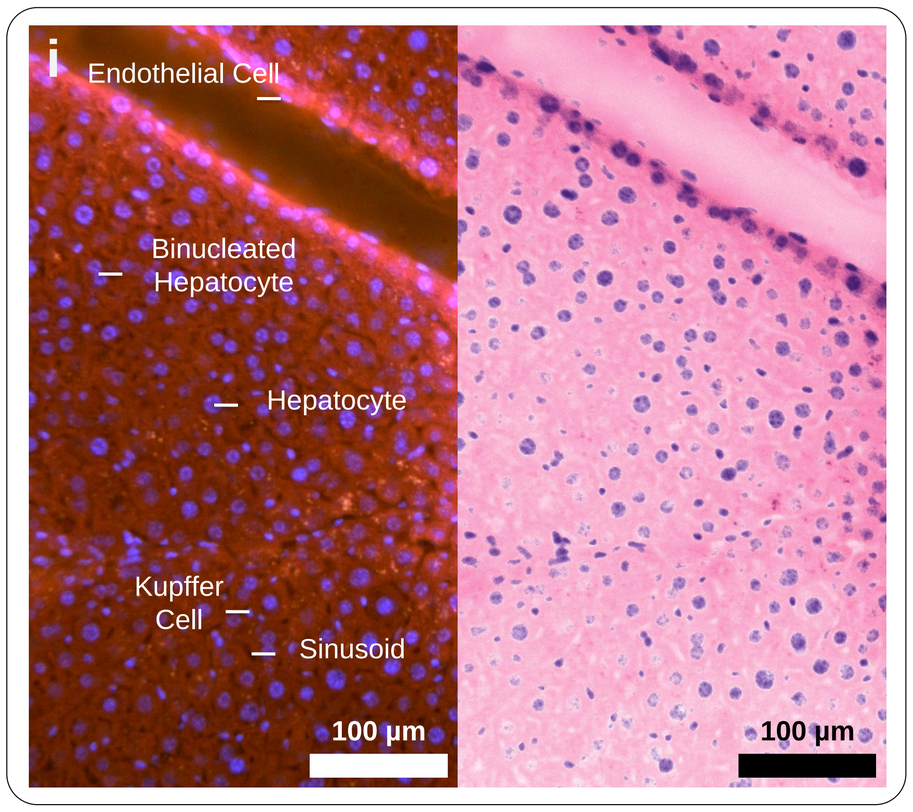
i
Endothelial Cell
Binucleated Hepatocyte
Hepatocyte
Kupffer Cell
Sinusoid
100 µm
100 µm

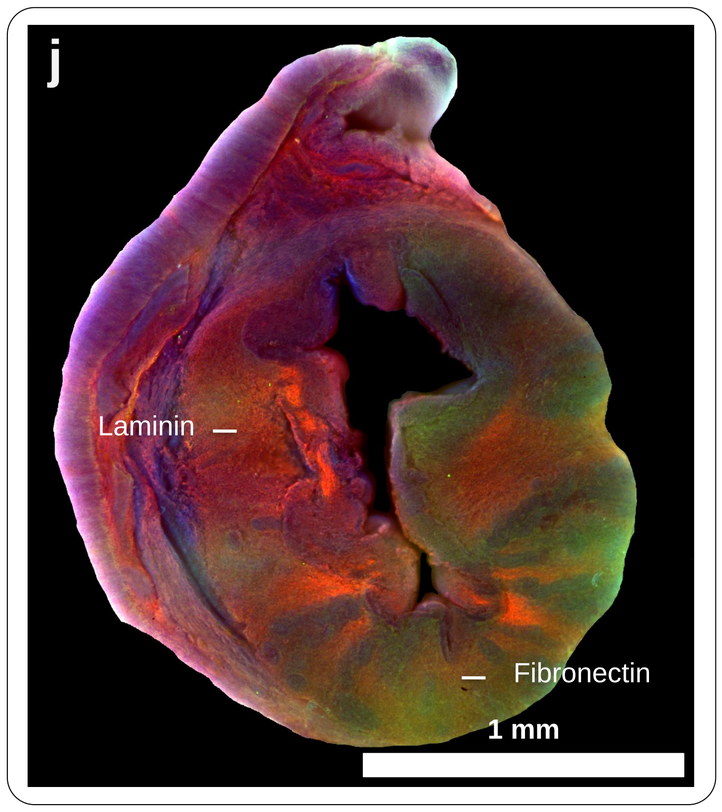
j
Laminin
Fibronectin
1 mm

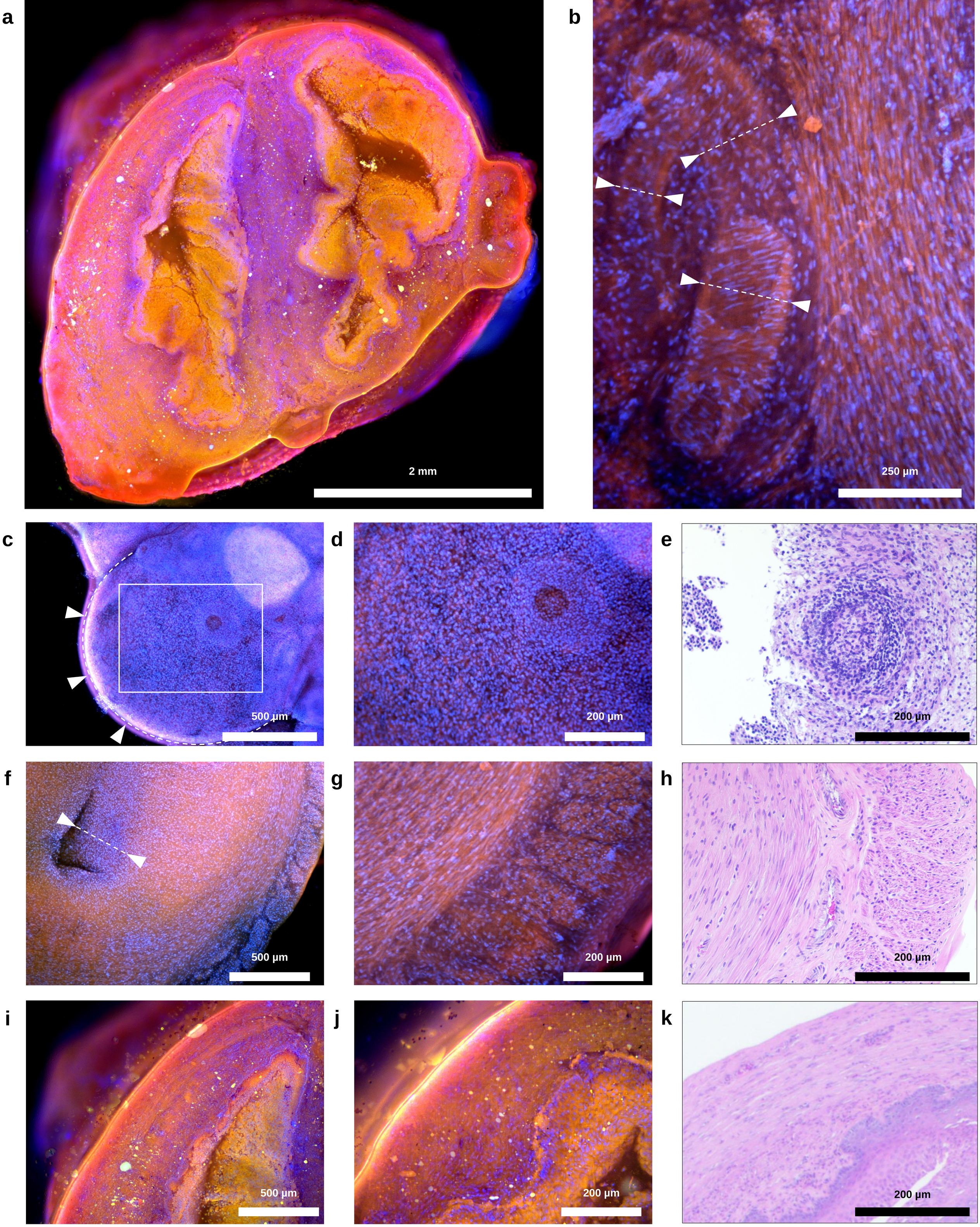
a
2 mm
b
250 µm
c
500 µm
d
200 µm
e
200 µm
f
500 µm
g
200 µm
h
200 µm
i
500 µm
j
200 µm
k
200 µm

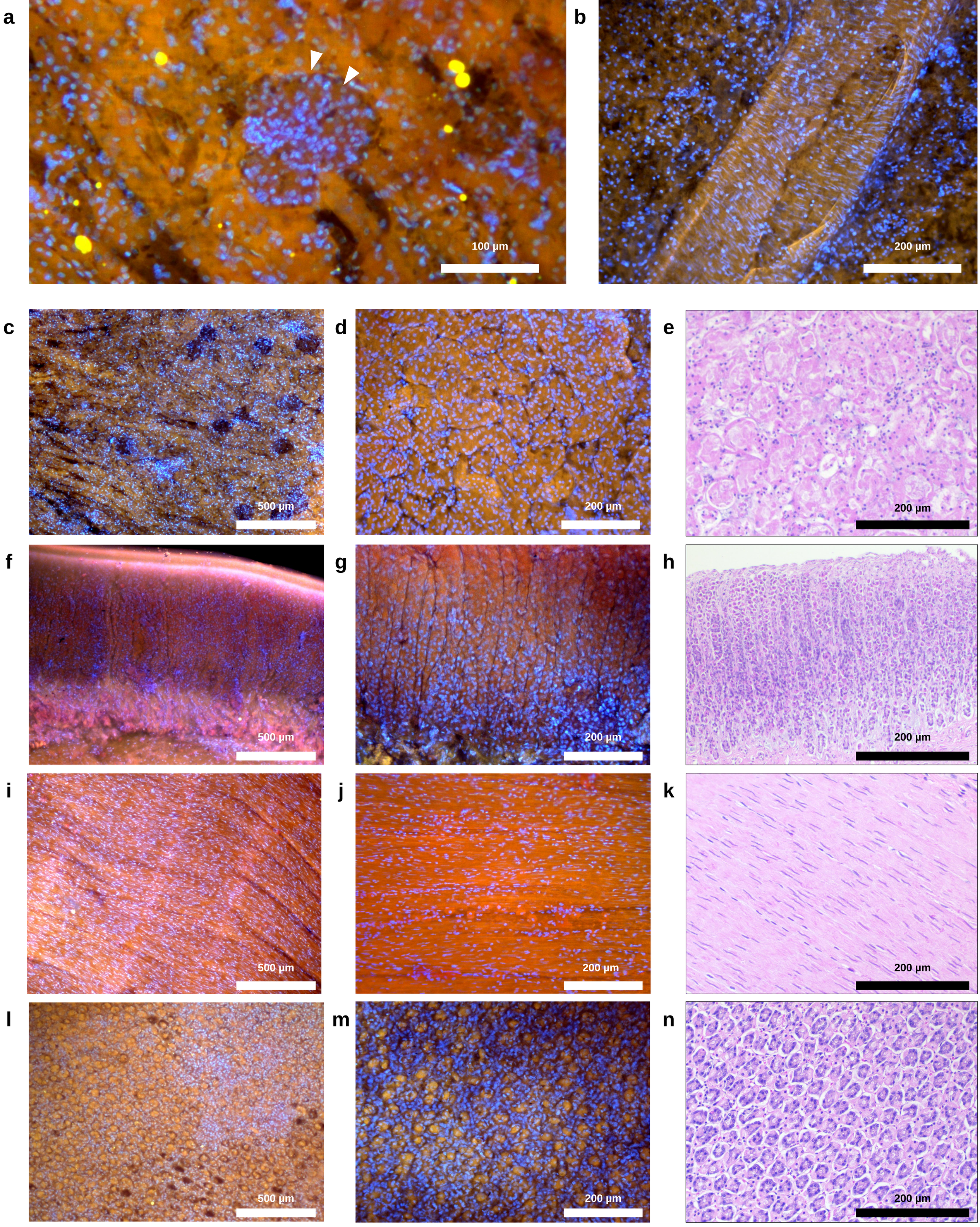
a
100 µm
b
200 µm
c
500 µm
d
200 µm
e
200 µm
f
500 µm
g
200 µm
h
200 µm
i
500 µm
j
200 µm
k
200 µm
l
500 µm
m
200 µm
n
200 µm

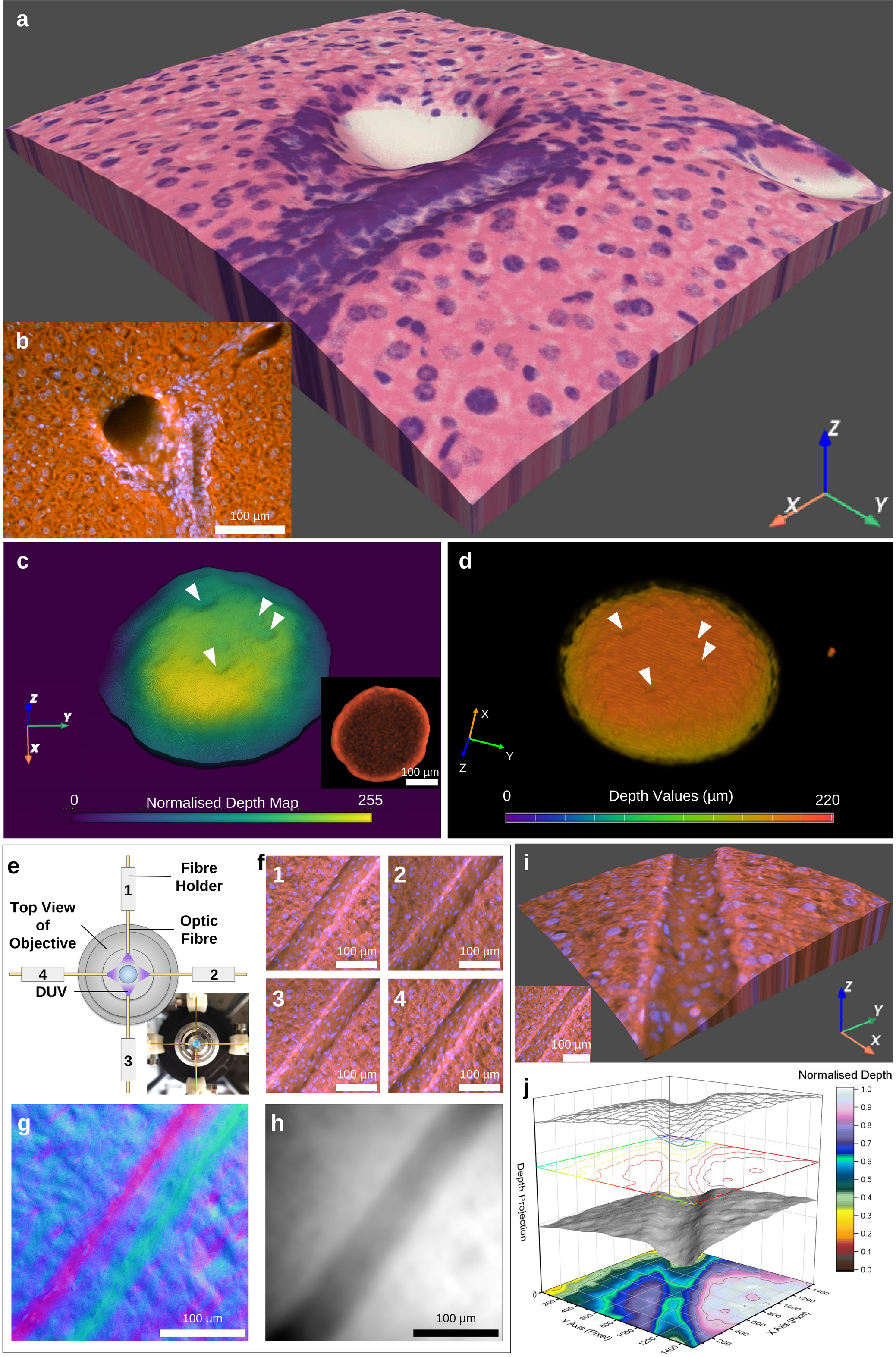
a
b
100 µm
Z
X
Y
c
Z
Y
X
100 µm
0
Normalised Depth Map
255
d
X
Y
Z
0
Depth Values (µm)
220
e
Fibre Holder
Top View of Objective
Optic Fibre
1
2
3
4
DUV
f
1
2
3
4
100 µm
i
100 µm
Z
Y
X
j
Normalised Depth
Depth Projection
Y Axis (Pixel)
X Axis (Pixel)
g
100 µm
h
100 µm

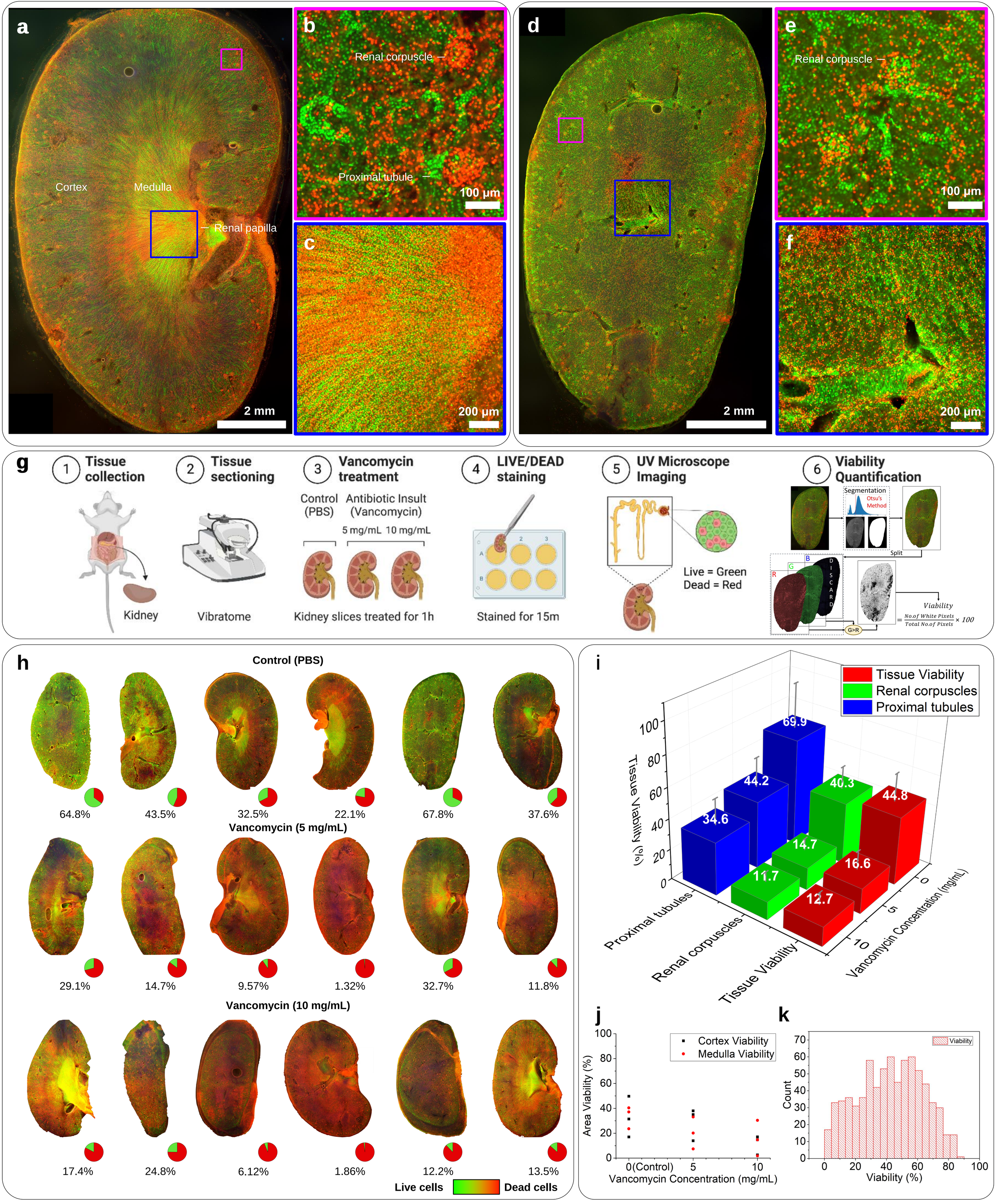
a
Cortex
Medulla
Renal papilla
2 mm
b
Renal corpuscle
Proximal tubule
100 µm
c
200 µm
d
2 mm
e
Renal corpuscle
100 µm
f
200 µm
g
1 Tissue collection
Kidney
2 Tissue sectioning
Vibratome
3 Vancomycin treatment
Control (PBS)
Antibiotic Insult (Vancomycin)
5 mg/mL 10 mg/mL
Kidney slices treated for 1h
4 LIVE/DEAD staining
Stained for 15m
5 UV Microscope Imaging
Live = Green
Dead = Red
6 Viability Quantification
Segmentation
Otsu's Method
Split
DISCARD
G>R
Viability = No.of White Pixels / Total No.of Pixels × 100
h
Control (PBS)
64.8%
43.5%
32.5%
22.1%
67.8%
37.6%
Vancomycin (5 mg/mL)
29.1%
14.7%
9.57%
1.32%
32.7%
11.8%
Vancomycin (10 mg/mL)
17.4%
24.8%
6.12%
1.86%
12.2%
13.5%
Live cells
Dead cells
i
Tissue Viability
Renal corpuscles
Proximal tubules
Tissue Viability (%)
69.9
44.2
34.6
40.3
44.8
14.7
16.6
11.7
12.7
Proximal tubules
Renal corpuscles
Tissue Viability
Vancomycin Concentration (mg/mL)
j
Cortex Viability
Medulla Viability
Area Viability (%)
0(Control)
5
10
Vancomycin Concentration (mg/mL)
k
Viability
Count
Viability (%)

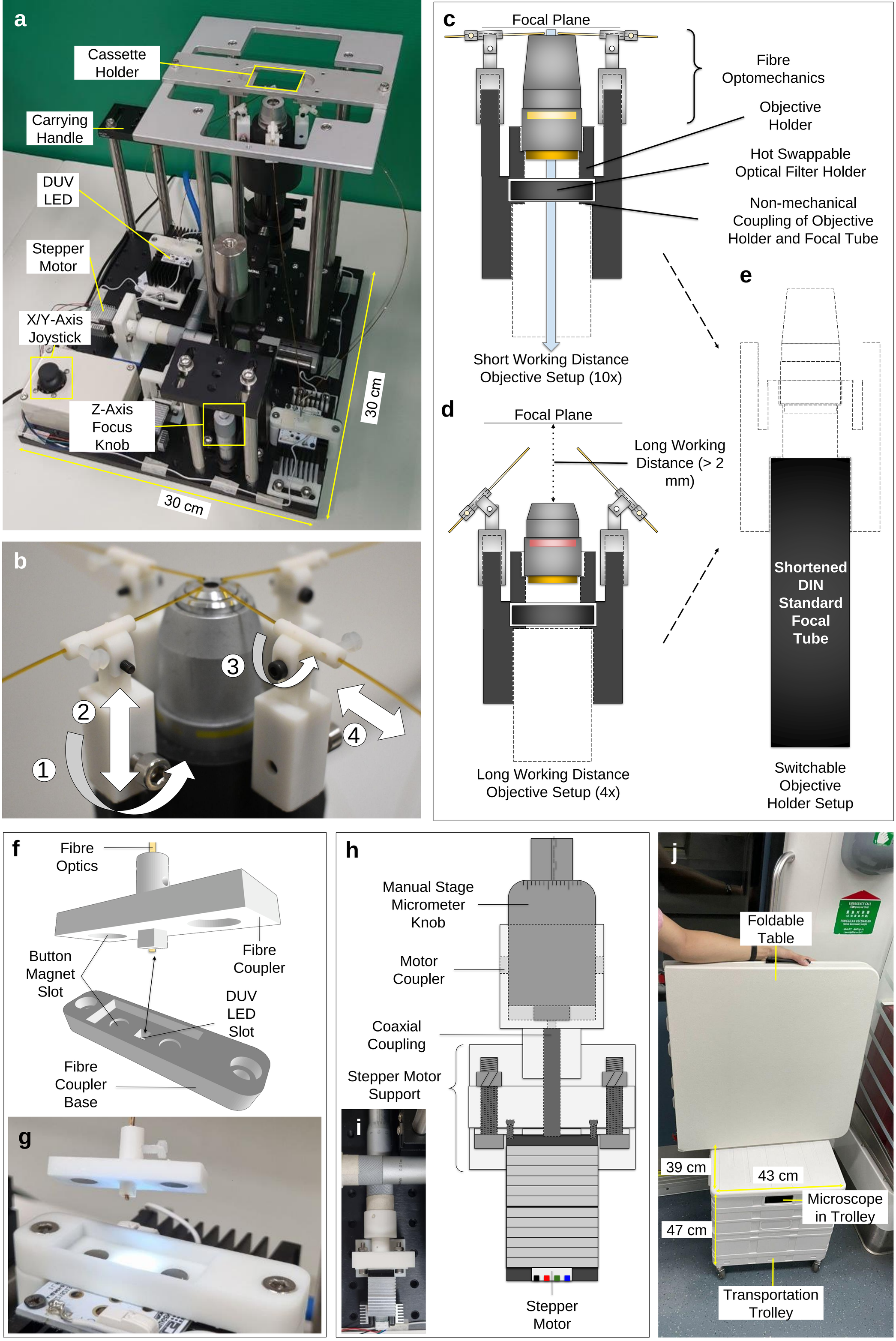
a
Cassette Holder
Carrying Handle
DUV LED
Stepper Motor
X/Y-Axis Joystick
Z-Axis Focus Knob
30 cm
30 cm
b
1
2
3
4
c
Focal Plane
Fibre Optomechanics
Objective Holder
Hot Swappable Optical Filter Holder
Non-mechanical Coupling of Objective Holder and Focal Tube
Short Working Distance Objective Setup (10x)
d
Focal Plane
Long Working Distance (> 2 mm)
Long Working Distance Objective Setup (4x)
e
Shortened DIN Standard Focal Tube
Switchable Objective Holder Setup
f
Fibre Optics
Button Magnet Slot
Fibre Coupler
DUV LED Slot
Fibre Coupler Base
g
h
Manual Stage Micrometer Knob
Motor Coupler
Coaxial Coupling
Stepper Motor Support
Stepper Motor
i
j
Foldable Table
39 cm
43 cm
47 cm
Microscope in Trolley
Transportation Trolley

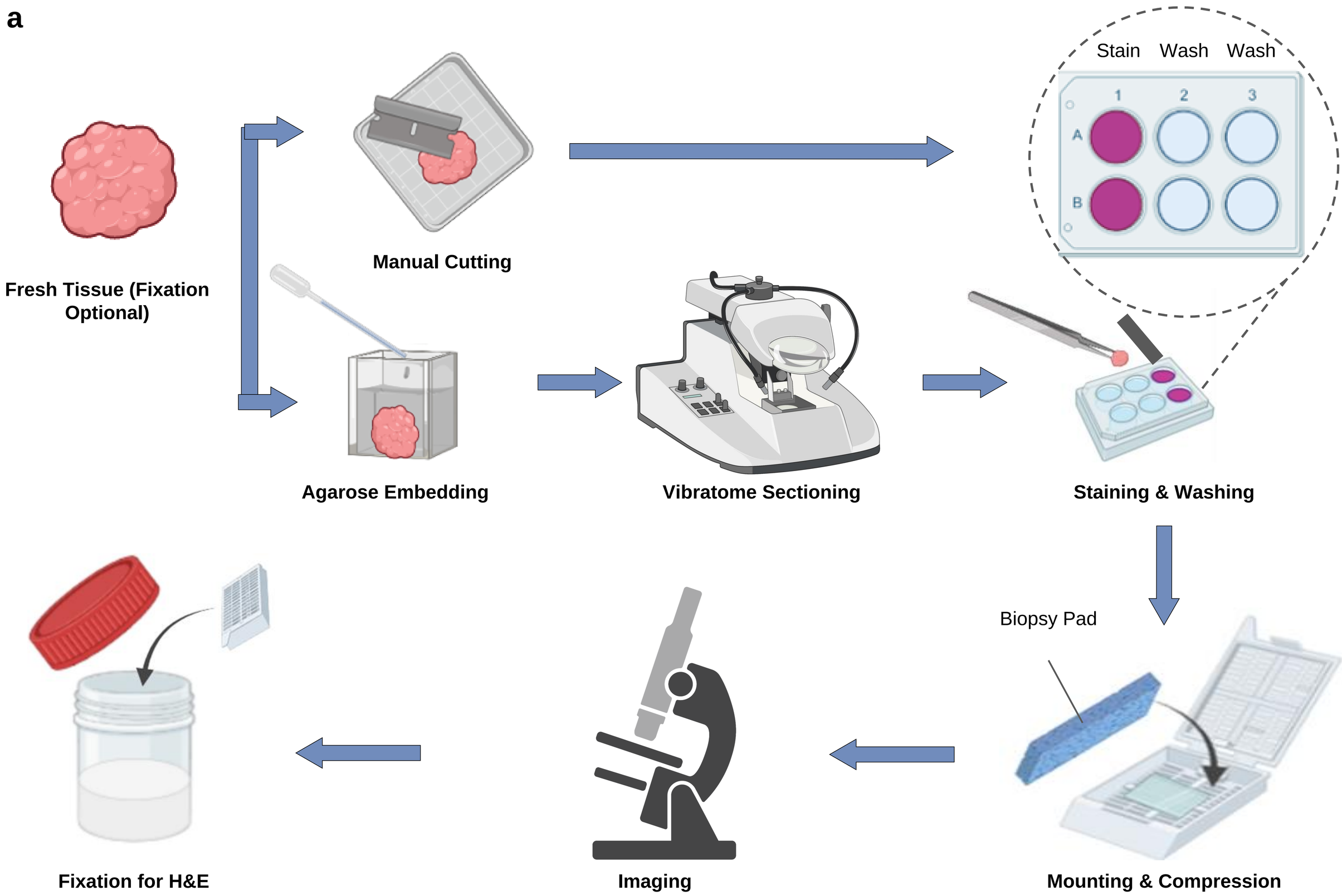
a
Fresh Tissue (Fixation Optional)
Manual Cutting
Agarose Embedding
Vibratome Sectioning
Stain
Wash
Wash
1
2
3
A
B
Staining & Washing
Biopsy Pad
Mounting & Compression
Imaging
Fixation for H&E

b
Surface
Transverse
Array